CLIMATOLOGY OF SYNOPTIC-SCALE ASCENT FOR WESTERN NORTH AMERICA: A PERSPECTIVE ON STORM TRACKS

by

Neil P. Lareau

A thesis submitted to the faculty of
The University of Utah
in partial fulfillment of the requirements for the degree of

Master of Science

Department of Atmospheric Sciences

The University of Utah

December 2010

The University of Utah Graduate School

STATEMENT OF THESIS APPROVAL

The thesis of **Neil P. Lareau**

has been approved by the following supervisory committee members:

John D. Horel	, Chair	**8/5/10** Date Approved
W. James Steenburgh	, Member	**8/5/10** Date Approved
Courtenay Strong	, Member	**8/5/10** Date Approved

and by **W. James Steenburgh** , Chair of

the Department of **Atmospheric Science**

and by Charles A. Wight, Dean of The Graduate School.

ABSTRACT

This study presents an ascent-based perspective on the climatology of storm tracks across western North America for the October-April cool seasons spanning 1989-2008. Data from the ECMWF ERA-interim reanalysis are used. Synoptic scale ascent is shown to be a physically significant measure of storm location and intensity that can be accumulated over seasonal time scales to represent storm tracks. Subsynoptic scale vertical motions, such as orographic ascent, are filtered by using an alternative balance version of the omega equation. This constraint is an important consideration to estimate storm tracks in regions of complex topography.

The climatological mean distribution of ascent suggests that the primary storm track occupies a sinusoidal belt across the eastern Pacific and adjacent portions of North America. The seasonal cycle in the location and intensity of storms is pronounced and consistent with synoptic experience. Interannual variations in synoptic-scale ascent are examined by principal component analysis. Meridional shifts from year-to-year of the locations of greatest ascent can be related to amplification and weakening of the climatological sinusoidal storm track. These interannual variations are found to be related to the phase of the El Niño Southern Oscillation, although the sample size of 19 seasons is a limitation for this analysis. The link between precipitation and synoptic-scale ascent is shown to be modulated by the extent to which the atmosphere is saturated.

TABLE OF CONTENTS

ACKNOWLEDGEMENTS

First and foremost I thank my adviser, Dr. John Horel, for his guidance, assistance, and patience throughout this study. I would also like to thank the other members of my committee, Drs. Jim Steenburgh and Courtney Strong, for their constructive criticisms and insights into this work. Special thanks are also in order for Rio Tinto whom generously supported this research project with a gift to the Department of Atmospheric Sciences. Additional support was provided by the NOAA CSTAR program under grant NA07NW34680003.

CHAPTER 1

INTRODUCTION

Background

The location, intensity, and frequency of transient synoptic-scale disturbances, or storms, have far reaching implications. Such storms represent an important component of the climate system on the global scale by transporting heat and moisture poleward, regulating the amount of cloudiness, and affecting the global hydrologic cycle. The role of these storms is no less important regionally. For western North America, cool-season storms contribute significantly to mountain snowpack, which in turn provides critical water resources for the subsequent summer months (Serreze et al. 1996). Significant shifts in the seasonal timing, location, or intensity of storms related to a warming global climate (Bengtsson and Hodges 2006) may have significant hydrologic consequences throughout the region. Secondary impacts may include variations in the strength and persistence of cold air pool events, which are common features in the quiescent interludes between storms and have significant impacts on regional air quality throughout the intermountain west.

Despite the far reaching impacts of synoptic-scale disturbances and numerous studies of storm tracks over the past half century, no clear picture has emerged regarding

the structure and variation in synoptic-scale pathways across western North America relative to the generally well-understood storm tracks across the Pacific Ocean. This lack of clarity is due, in part, to the influence of terrain on the myriad techniques used to define storms and storm tracks combined with the complexity of terrain-flow interactions on all scales of motion. For example, near-surface storm metrics, such as cyclone tracking procedures, tend to show discontinuous storm tracks across interior western North America (Jeglum and Steenburgh 2010) while examination of mid- and upper-tropospheric vorticity features exhibit more continuous tracks (Lefevre and Nielsen-Gammon 1995; Hoskins and Hodges 2002). Yet, even amongst studies that rely on mid- and upper-tropospheric fields, the latitude of the mean synoptic pathway varies from 30°N to 55°N (Blackmon 1976, Hoskins and Hodges 2002) and spatial patterns vary from zonal (Blackmon 1976) to amplified sinusoidal pathways (Hakim 2000). Furthermore, few studies (Myoung and Deng 2009; Wettstein and Wallace 2010) have explicitly examined interannual variations in regional storm tracks or the links between them and planetary-scale variations such as the El Nino Southern Oscillation (ENSO) phenomenon.

Prior storm-track studies have also tended to focus on aggregated statistics obtained from specific metrics and then relied on conceptual models of synoptic-scale systems to interpret impacts on sensible weather for the ‘ideal’ or ‘typical’ case. This approach tends to ignore the considerable variability in precipitation and cloudiness within, for example, samples of events of closed cyclonic circulations or open wave troughs. The association of sensible weather to cumulative statistics obtained from variance-based methods often used to define storm tracks is even less clear, since the requisite time scales and sample sizes used in averaging provide limited insight to

interpret individual events. In contrast, case studies of mid-latitude weather systems tend to focus on the dynamics contributing to the sensible weather, including diagnosis of synoptic-scale ascent (Hoskins et al 1978; Hoskins and Pedder 1980; Keyser et al 1988; Martin 2007; West and Steenburgh 2010), which has profound impacts on precipitation, cloudiness, and the structure of the storm itself (Durran and Snellman 1987; Martin 2007). Storm-track studies could benefit from employing similar dynamically based diagnosis.

In light of potential shifts in storm tracks due to anthropogenic climate change, the ambiguities in our present understanding of the distribution of storms over complex topography, and the sensitivity of the interpretation of sensible weather associated with storm tracking methodology, the purpose of this study is to provide a physically significant, dynamically filtered, and weakly constrained measure of storm tracks across western North America. Physical significance is established by a novel synoptic-scale ascent-based measure of storm location and intensity. Values of ascent are subsequently dynamically filtered, so as to remove mesoscale motions, through the use of an alternative balance equation for vertical motions and the metric is weakly constrained so as to be inclusive of a range of synoptic features such as cyclones, open wave troughs, and frontal systems. Measures of storm track behavior over the span of an individual storm, month, season, or climatological period are obtained by accumulating at 6-hr intervals the column maximum contribution of synoptically-forced ascent during cool seasons (October-April) 1989-2008. Subsequently, modes of interannual variability in the ascent-based storm tracks are examined by means of principal component analysis (PCA), the results of which are linked to the El Niño Southern Oscillation (ENSO).

This thesis is organized as follows. The remainder of Chapter 1 will review pertinent literature. Chapter 2 will provide details on the data sets and methods employed and Chapter 3 will demonstrate the methodology used to calculate synoptic-scale vertical motions. Statistical summaries will be provided in Chapter 4, and the implications of these findings will be addressed in Chapter 5. The last chapter will summarize the results.

Prior Research

There is a rich history of research concerned with the distribution of synoptic-scale transient disturbances and their favored locations, or storm tracks, generally examined separately in terms of lower-, mid- or upper-tropospheric phenomena. The specific techniques used to examine these phenomena tend to fall into two major categories: (1) feature based, in which features (i.e., cyclones) are identified and their location and attributes are tracked through space and/or time and (2) filtered variance, wherein tropospheric fields, such as geopotential height, are filtered on synoptic temporal and/or spatial scales.

Feature based studies may be further divided into Lagrangian, or feature following, and Eulerian, or grid point, based studies (Hoskins and Hodges 2002). While these two techniques differ markedly, Lagranian statistics are ultimately presented in many publications within an Eulerian frame work wherein the frequency of occurrence of a feature, or that feature's track, is examined at each grid point. The following review will primarily focus on the Eulerian aspects of feature based studies.

Lower Troposphere

Interest in preferred storm tracks originated with early studies of Atlantic cyclones, which were seen to be responsible for the preponderance of sensible weather. Numerous studies have since examined the Northern Hemisphere distribution of cyclone tracks, typically identifying and tracking closed contours in sea level pressure (SLP). A small subset of these studies is relevant to western North America. Reitan et al. (1974) provide a cyclone frequency climatology for the North American continent and adjacent oceanic domain based on cyclone track data from the National Weather Service. A northern track roughly parallel to the United States/Canadian border was evident during January with cyclogenesis events strongly favoring the lee side of the Rocky Mountains in both Alberta and Colorado. During April, a track from the Gulf of Alaska east through British Columbia was found in addition to a region of high cyclone frequency anchored in southeastern Colorado and extending northeast to the Great Lakes. Cyclogenesis during April was maximized in a swath across the southwestern US and extended to an absolute maxima in Colorado.

Zishka and Smith (1980) developed a cyclone climatology for the months of January and July based on National Oceanographic and Atmospheric Administration (NOAA) Environmental Data Service cyclone track maps spanning 1950-1977, which is consistent in many respects with the climatology of Reitan et al. (1974). In addition to the total cyclone counts, a metric was introduced to delineate regions where the interannual variation in the number of cyclones is low yet the total storm count is high, suggesting persistent pathways for these mobile systems. For January, both the cyclone counts and regions of low ‘relative variability’ correspond well with the northern track demonstrated

by Reitan et al. (1974). The Intermountain West is characterized by infrequent cyclones and high relative variability.

While Zishka and Smith (1980) only addressed cyclone distributions for January and July, Whittaker and Horn (1981) provided a more comprehensive treatment of the seasonal cycle of cyclogenesis, although they did not explicitly address cyclone tracks. Similar to Reitan et al. (1974), the intermountain west has a cyclogenesis peak in April. Colorado cyclone formation was found to be favored during March. For the domain as a whole, cyclogenesis was more frequent during the late winter before diminishing and migrating north during the boreal summer.

With the availability of reanalysis products as well as the prospect of shifts in storm tracks due to a warming climate, a renewed focus during the past ten years has been applied to deduce the distribution of cyclones. As a portion of a comprehensive survey of numerous measures of storm tracks for the Northern Hemisphere, Hoskins and Hodges (2002, hereafter HH), presented feature-tracking climatologies for SLP minima and 850 hPa relative vorticity maxima (comparable to tracking surface cyclones) in the European Center for Medium-Range Weather Forecasts (ECMWF) ERA-15 reanalysis during 1979-2000. HH used two primary measures of storm tracks for these lower tropospheric fields: (1) feature density and (2) track density. Feature density is biased somewhat towards slowly moving systems that make large contributions to total density, while track density focuses on the contribution from a single system. The track and feature densities for SLP are both qualitatively similar with the results of Reitan et al. (1974) and Zishka and Smith (1980) with a northern storm track consisting of tenuously-connected maxima across the Canadian Rockies, a local maximum just downstream of

the Rocky Mountains in Colorado, and high densities in the Gulf of Alaska. The mean intensity for SLP features shows a tongue of locally high intensity systems extending from the Pacific Northwest through the Intermountain West and onto the high plains of Colorado, indicating that the relatively weak track densities for the Intermountain region may correspond to strong systems. Although SLP and 850 hPa relative vorticity yield broadly similar results for the hemisphere as a whole, significant differences can be found across western North America. The 850 hPa relative vorticity statistics exhibit near zero densities for tracks and features over elevated topography while a coastal band of higher feature and track densities extends south to Baja California. The mountain minima and coastal maxima were not seen in the SLP diagnostic.

Following a methodology developed by Blackmon (1976), HH also employ a 2-6.5 day filtered variance (standard deviation) metric for SLP and 850 hPa relative vorticity, the results of which are similar to the above tracking statistics. SLP variance maximizes near 50° N and is connected to upstream and downstream maxima over the Pacific and North Atlantic, respectively. There is a 'ridge' of zonally minimized variance centered on the western coast of North America, suggestive of the mean climatological ridge in geopotential heights. By comparison, variance in 850 hPa relative vorticity is everywhere minimized over the axis of the Rocky Mountains, showing no semblance of a west-to-east connected storm track, a result which is similar to the tracking statistics. However, the 850 hPa vorticity variance does not indicate the elongated coastal maxima present in the vorticity tracking version. In understanding these results, it should be remembered that the SLP and 850 hPa relative vorticity fields require vertical interpolation over the western United States due to the elevated landmass, which calls

into question their appropriateness for the region. Track smoothness and duration requirements may also play a role in these differing statistics.

Noting the difficulty of using extrapolated fields in the presence of complex elevated topography, Wernli and Schwierz (2006) excluded much of the western US from a recent hemispheric climatology of SLP cyclones using the ERA-40 reanalysis. However, the western US domain was subsequently examined by Jeglum et al (2010, hereafter JM), who relied on multiple reanalysis products (NARR, ERA-40, ERA-interim) and both the SLP and 850 hPa geopotential height fields to examine cyclone density. While the results of their study were found to be sensitive to the model resolution (with higher resolution products yielding higher cyclone counts), a consistent picture of multiple local maxima in cyclone density within the intermountain region was found. Furthermore, the total cyclone counts in the intermountain region were found to be comparable in magnitude to that in the eastern Gulf of Alaska, which suggests previous cyclone studies without an intermountain maximum may have suffered from data sparseness or coarse grid scales. Although HH did find a weak center of storm activity in the intermountain west, JM indicates this maximum is located further south, roughly in the lee of the southern portion Sierra Nevada Mountains, which is in closer agreement to the distribution previously found by Klein et al. (1968). They examined twice daily National Meteorological Center (NMC) analyses during winter from 1951-1964 and identified closed centers of circulation at four pressure levels (850, 700, 500, and 300 hPa) for a domain centered on the intermountain west. Feature density at 850 hPa showed numerous local maxima with the highest densities immediately downstream of the Rocky Mountains and secondary maxima located from the Gulf of California extending north

along the tri-state junction of California, Arizona, and Nevada (which is near the maxima also seen by JM). The distribution of upper level features was somewhat different with highest densities found near the northern Gulf of California.

In one of the few cyclone studies to consider interannual variability, Myoung and Deng (2009) presented a coastal cyclone activity function (CAF), which is a one dimensional measure for cyclones along the western coast of North America. Year-to year-changes in the CAF were presented in terms of the leading PCA modes of variability. Their second mode exhibits a north-south dipole pattern, the time series of which was correlated with sea surface temperature in the Nino 3.4 region. Myoung and Deng (2009) also examined the fraction of winter season precipitation for the western US that could be attributed to coastal cyclones as well as how the modes of cyclone variability related to variations in regional precipitation. Their findings demonstrate that coastal precipitation is strongly linked to coastal cyclones while precipitation in the interior western US is less directly associated with these oceanic storms.

Mid Troposphere

An alternative perspective on storm tracks is obtained by analyzing mid-tropospheric phenomena. Blackmon (1976) filtered the 500 hPa geopotential height field over the northern hemisphere so as to isolate synoptic-scale transients, which were generally assumed to lie within frequencies of 1-6 days and within zonal wave numbers, n, between 7-18. For a subset of medium waves ($7<n<12$) within the 2.5-6 day band, the resulting ‘storm track’ was seen to be more or less zonal and centered near 42º N with strong connectivity across the western United States. These results contrast with all of the

aforementioned cyclone studies, which showed only tenuous continuity across this same region. Shorter waves (13<n<18) within the same timescale had centers of high variance further north, with a weak connection across the Canadian Rockies near 55° N, whereas short-wave features within the 1-2 day temporal band showed a stronger connection across this same region. Blackmon (1976) also presented a climatology of 500 hPa vorticity features wherein high values of cyclonic vorticity tended to correspond to regions of high filtered variance over northern potions of the domain, although cyclonic vorticity features were also common across the southwestern US where variance was generally low. The presence of strong southern vorticity maxima is, however, roughly in agreement with cyclone density centers observed by JM as well as by Klein et al. (1968).

HH also extended their storm track analysis by using filtered variance and tracking of 500 hPa omega features (vertical motions). Variance is maximized in a roughly zonal band, centered near 33° N, which possesses a weak sinusoidal meander from the eastern Pacific across the western US. The position of this inferred omega storm track is considerably south of that found from lower tropospheric variance studies, as well as the variance documented by Blackmon (1976), which maximized between 45° N and 55° N. The tracking statistics for 500 hPa omega yield a less continuous pathway. Track density is minimized over the continental divide and exhibits more strongly meridional features as compared to the variance metric. Specifically, a northwest-southeast maximum in track density was found along the northwest coast of North America, which then extends inland towards Arizona. The HH results obtained from the 500 hPa omega metrics bear some similarity to those employed in the present study and will be discussed further in Chapter 5.

The variance of geopotential height is presumed to be closely related to the presence of troughs on the 500 hPa surface, climatologies of which have been compiled by Sanders (1988), Lefevre and Nieslon-Gammon (1995; hereafter LNG), Dean and Bosart (1996), and Hakim (2000; hereafter HK). Sanders (1988) subjectively tracked troughs in terms of the 552 dam contour of the 500 hPa surface during nine cold seasons (Oct-May 1976/1977 – 1985/1986). Results were presented in the context of tough-lysis and trough-genesis and generally showed an excess of trough-lysis events upstream of the Rocky Mountains and genesis events downstream. Little information about the overall density of these features was provided in that study. In a comprehensive and objective climatology of 500 hPa troughs, LNG defined the Eulerian centripetal acceleration (ECA) as the product of the geostrophic wind and the geostrophic curvature vorticity. Maximum values of ECA are typically collocated with tough axes in the height field, and thus ECA serves as an objective measure of trough location and intensity that can be readily tracked. The resulting track statistics for western North America showed a connected region of maximized feature frequency that meanders south from the Gulf of Alaska to northern Baja California, before turning zonally along the US/Mexico border, and then northeast towards the Great Lakes. Local maxima were found within the ‘storm track’ in the Gulf of Alaska, west of Baja California, and over the Great Lakes. A weak indication of a more northern track was evident across southern British Columbia.

Dean and Bosart (1996) provide a similar perspective on 500 hPa trough distribution as a portion of a hemispheric study on trough merger and fracture. Using a trough identification criteria based on closed circulation centers, defined as local maxima in geostrophic absolute vorticity relative to a zonal base state, the total number of trough

occurrences was presented from September 1957 through May 1989. A strong maximum in occurrence was found over the Gulf of Alaska with a local maximum over southern California and a weak track across the Canadian Rockies proximal to the US border. There is also a local maximum found near southeast Colorado and the northern panhandle of Texas.

Approaching 500 hPa trough distributions from a potential vorticity (PV) perspective, HK developed a climatology of 500 hPa relative vorticity maxima for 33 winter seasons (December-January-February 1957-1989). The PV framework, explored at length by Hoskins et al. (1985), is one in which downward deflections of the dynamic tropopause surface (1.5 Potential Vorticity Units (PVU) in this case) are seen as the source of strong cyclonic relative vorticity features in the mid troposphere. The climatology of vorticity maxima presented by HK is given as the percentage of the total number of time steps for which a vorticity maximum is present at a grid point as compared to the total number of time steps during the study period. As such, these results are not identical to tracking statistics, but nonetheless provide a sense of synoptic pathways. Results are divided into the distribution of vorticity features within four ascending classes of intensity. Moderate (4×10^{-5} $s^{-1} \leq \zeta_g \leq 4 \times 10^{-5}$ s^{-1}) 500 hPa relative vorticity frequency was shown to be maximized in a connected band from the Gulf of Alaska eastward into the Canadian plains, with an embedded maximum in the lee of the Canadian Rockies. The distribution of strong and extreme vorticity (8×10^{-5} $s^{-1} \leq \zeta_g \leq 30 \times 10^{-5}$ s^{-1}) features was quite different, showing a connected maxima of high frequency from the Gulf of Alaska south along the Pacific seaboard, then curving east across the northern Gulf of California, and eventually northeast into the central US. Embedded

maxima were found both in the Gulf of Alaska and the Gulf of California regions. The Gulf of California maximum was comparatively stronger when only extreme events were considered. This distribution of synoptic pathways is spatially similar to that documented by both LNG and Dean and Bosart (1996). Not surprisingly, this distribution is also similar to the 500 hPa vorticity climatology included by Blackmon (1977).

The connection between upper-level tropopause features and mid-tropospheric response has also been provided by Elbern et al. (1998). Joint occurrences of the intersection of the 1.6 PVU surface with the 400 hPa level combined with strong values of divergent Q-vectors (representing downward motions) were documented. This dual criterion was designed to identify subgrid scale tropopause folds in coarse gridded analysis products and was tested against higher resolution mesoscale simulations. The tropopause fold distribution during winter was spatially similar to the vorticity distribution documented by HK, with a local maximum over the northern Gulf of California. Results from both Elbern et al. (1998) and HK will be discussed further in Chapter 5.

Upper Troposphere

HH presented a number of upper-tropospheric fields that were both tracked and analyzed in terms of variance methods. These fields include geopotential height and relative vorticity at 250 hPa, potential vorticity on the 330 K isentropic surface, and potential temperature on the 2 PVU surface. The two variance measures on the 250 hPa surface both show a continuous storm track across western North America, but differences in the north-south location of the tracks are not trivial. Variance in the height

field exhibits a broad connected maximum centered near 50° N, while the narrower region of maximum vorticity variance is centered further south at roughly 42° N. Both fields are more or less zonal in the distribution of large variances and show lower maximum values proximal to the Rocky Mountains. In contrast, the variance of the potential vorticity on the 330K isentropic surface has a local maximum over the Intermountain West, which is embedded within a connected ribbon of maximized variance centered near 43° N. The Intermountain West variance maximum is larger than any values found upstream over the Pacific, though still lower than those found in the Atlantic storm track. Yet another perspective is provided by the variance in the potential temperature of the dynamic tropopause surface, which shows an elongated Pacific maximum that extends zonally into the southwestern US near 30° N.

HH tracking statistics for each of the above fields do not consolidate into a single high altitude storm track. Track densities for negative 250 hPa height anomalies are located somewhat south of the variance maximum for the same field. The connectivity of the track across the region is modest, showing numerous local maxima within the western US, including a well-defined maximum in the lee of the Rocky Mountains. The relative vorticity track density is considerably different than both the associated variance field and the related 250 hPa height fields. Specifically, the track density exhibits a sinusoidal pattern wherein maxima are displaced north near the Pacific Northwest and then south towards the Gulf of California before turning east and northeast into the central US. There is a weaker connected track just north of the US/Canadian border. This perspective is strikingly similar to the HK 500 hPa relative vorticity frequency, yet unlike all of the

other upper tropospheric fields. Tracking statistics for PV 330K and potential temperature at 2 PVU show reasonable agreement with their associated variance fields.

Summary

Overall, no unified view of storm tracks across western North America emerges on the basis of the various procedures, variables, and levels examined. One interpretation for this diversity is that different dynamical processes are taking place in the lower, mid, and upper troposphere and those are manifested in different ways. For example, it seems intuitive to expect that mid- and upper-tropospheric fields will tend to be more connected since open wave features at those levels tend to propagate in a coherent fashion across western North America whereas near-surface fields tend to be heavily influenced by the underlying terrain. The physical phenomena of interest also impose differences in the apparent storm track. Surface cyclones, which require a spin-up time to generate a closed circulation, are inherently more discontinuous in space and time than features that are approximately conserved quantities (e.g., absolute and potential vorticity). Finally, most of the techniques used to identify storm tracks can only be related tenuously to sensible weather such as cloudiness or precipitation. The following chapters will attempt to provide a clearer interpretation of the occurrence of synoptic-scale ascent and thereby provide a novel estimate of storm tracks across western North America.

CHAPTER 2

DATA AND METHODS

Reanalysis Data

Data from the European Center for Medium Range Weather Forecasts (ECMWF) ERA-Interim global reanalysis provide the four-dimensional representation of the state of the atmosphere used in this study. The ERA-Interim is a state of the art reanalysis system that covers the 'data rich' period from 1 Jan. 1989 through the present. Analyses are produced using the Cy31r1/2 version of the ECMWF Integrated Forecasting System (IFS) configured with a T255 triangular truncation horizontal grid and 60 vertical levels (ECMWF newsletter 110,111,115,119). The analysis system employs a four-dimensional variational assimilation (4D-Var) system that assimilates a broad range of observations within a 12-hour window. Data sources include cloud-track winds, satellite radiances, satellite scatterometer winds, radio-occultation measurements (since 1996), surface observations (wind, temperature, pressure, and humidity), operational radiosonde data, altimeter wave heights, and ozone profiles. Significant improvements over past ECMWF reanalysis products (ERA-40, ERA-15) are due in part to the improved 4D-Var system and improved model physics but also due to a variational bias correction system. As described by Dee and Uppala (2009), variational bias correction helps to maintain

consistency in the analyses in the presence of ‘data events’ wherein the number and quality of observations changes in time, including the introduction of new data streams.

The quality of the reanalysis over the western United States depends on the model’s resolution (~80 km) of the complex topography of the region (Fig. 2.1a). A qualitative comparison of the ERA-interim terrain to that obtained from a 1/3° (~36 km) digital elevation model (Fig. 2.1b) suggests that the ERA-interim coarsely represents the regional orography, failing to resolve important features such as the highest portions of the Sierra Nevada Mountains near their southern terminus in California. Terrain smoothing is evident as well elsewhere in the domain such as central Nevada, where the cross barrier scale of individual mountain ranges is small.

The gridded model data used in this study were obtained from the ECMWF data server (http://data-portal.ecmwf.int/data/d/interim_daily/). The region bounded by 22-58° N and 70-160° W (Fig. 2.1a) was selected for this study and covers the majority of the contiguous United States and an adjacent portion of the eastern Pacific Ocean. Post-processed geopotential, temperature, relative humidity, zonal and meridional wind, vertical velocity, and relative vorticity are provided at 6 hourly time steps while accumulated precipitation is available at 12-hour intervals. Dynamic fields are available on 37 isobaric surfaces at a reduced horizontal resolution of 1.5° (~165 km). Although additional levels will be used in Chapter 3 to evaluate the analysis approach, this study focuses most heavily on five isobaric surfaces (700, 600, 500, 400, 300 hPa) with the lowest pressure surface, 700 hPa, above the model’s terrain except for a single gridpoint in central Colorado.

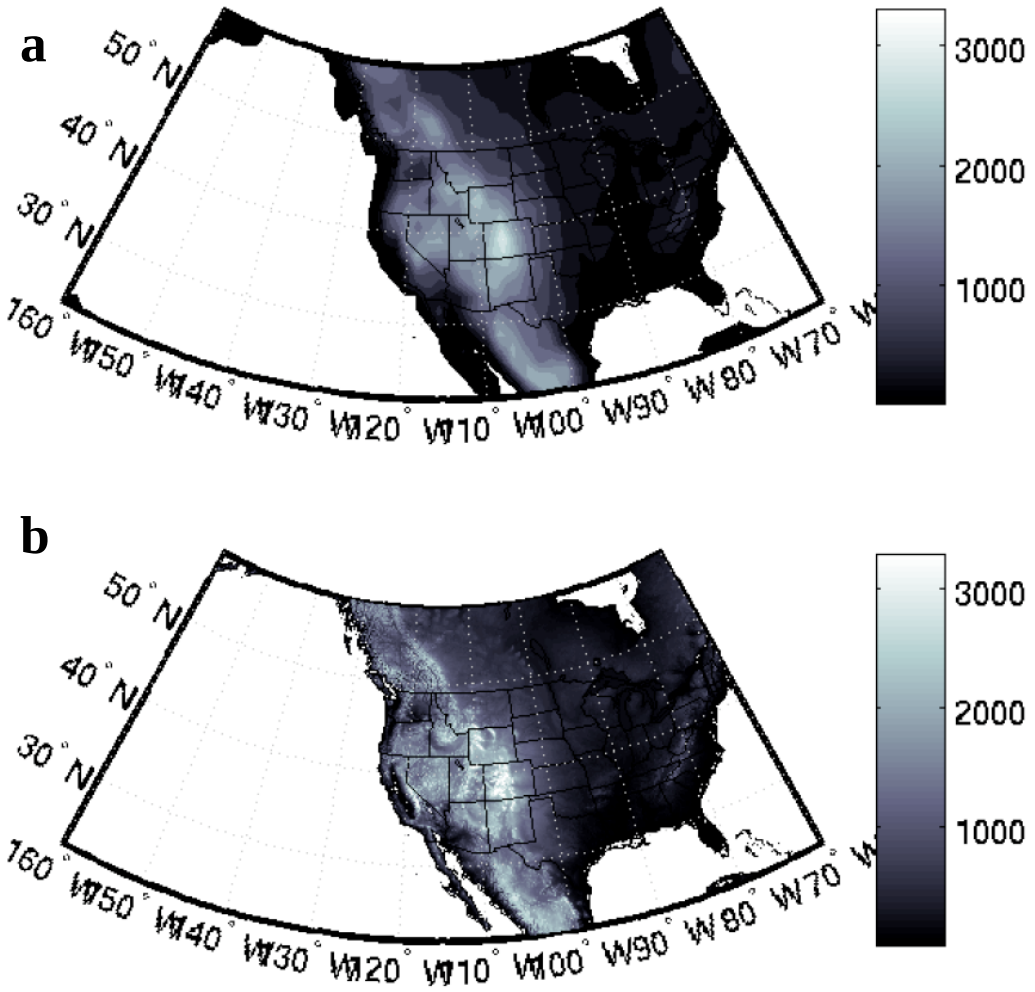

Figure 2.1. North Americans study domain and topography. (a) ERA-interim 1.5° topography. (b) 30-arc second topography.

Computing Vertical Motion

The spatial and temporal distribution of synoptic-scale vertical motions can be used to characterize mid-latitude weather systems, or storms. Ascent, in particular, is of profound importance, providing the supersaturation necessary for precipitation and clouds (Rose and Lin 2003) as well as altering the environmental lapse rate, which in turn may favor mesoscale vertical motions (Durran and Snellman 1987). Furthermore, differential vertical motions can act to stretch columns of air vertically affecting the distribution of relative vorticity, a process that can lead to storm intensification (Martin 2007). Using quasi-geostrophic (QG) reasoning, vertical motions are viewed as part of a secondary ageostrophic circulation that maintains the thermal wind and hydrostatic balance of the primary geostrophic flow (Hoskins et al. 1978; Hoskins and Pedder 1980; Durran and Snellman 1987). These vertical motions are commonly viewed as being synoptically "forced" vertical motions exhibiting a typical scale of 10^{-2} m s^{-1} (~-.1 Pa s^{-1}), which is 3 orders of magnitude smaller than QG scaling assumptions for horizontal motions (10 m s^{-1}).

Numerous formulations of the QG omega equation have been devised starting with Sutcliffe (1947), revised and simplified to eliminate term cancelation by Trenberth (1978), and addressed at length by Hoskins et al. (1978) and Hoskins and Pedder (1980) who introduced the concise Q-vector notation. Subsequently, Robert Davies-Jones (1991; 2009) presented a generalized version of Hoskin's Q-vector omega equation. Specifically, Davies-Jones (1991; 2009) demonstrated that an alternative balance form of the omega equation that reflects a closer approximation to the full primitive equations omega can be obtained by substituting the nondivergent component of the observed wind

for the geostrophic wind in the calculation of the Q-vector. A similar approximation was previously employed by Keyser et al. (1988) to generalize the Petterssen frontogensis function in a Q-vector framework. The present study follows the conceptual frame work of the Hoskin's Q-vector approach but uses the Davies-Jones substitution of the nondivergent wind field in place of the geostrophic wind in order to estimate synoptic-scale vertical motions. This approach will henceforth be referred to as the alternative balance (AB) omega equation.

The numerical method detailed by Krishnamurti and Bounoua (1995) is followed to obtain the nondivergent wind, wherein the ERA-interim wind field is split into the areal average, nondivergent, and irrotational components:

$$\vec{V}_{total} = \vec{V}_{mean} + k \times \nabla\psi + \nabla\chi \tag{2.1}$$

where ψ is the streamfunction and χ is the velocity potential. Ignoring spherical geometry:

$$\nabla^2\psi = \zeta = \frac{\partial \mathrm{v}}{\partial x} - \frac{\partial \mathrm{u}}{\partial y} \tag{2.2}$$

$$\nabla^2\chi = -\left(\frac{\partial \mathrm{u}}{\partial x} + \frac{\partial \mathrm{v}}{\partial y}\right) \tag{2.3}$$

Thus, by using the relative vorticity (ζ) calculated from the ERA-interim wind field, we may solve for ψ on each pressure level using a successive over-relaxation algorithm. Having obtained ψ, the nondivergent components of the wind are then

$$u_\psi = -\frac{\partial \psi}{\partial y} \tag{2.4}$$

$$v_\psi = \frac{\partial \psi}{\partial x} \tag{2.5}$$

An example of this decomposition is provided in Chapter 3**.**

Using the nondivergent component of the observed wind, the generalized version of the Q-vector form of the omega equation is:

$$\sigma \nabla_{\mathrm{p}}{}^2 \omega + f_0 \frac{\partial^2}{\partial \mathrm{p}^2} \omega = -2 \nabla_{\mathrm{p}} \cdot \vec{\mathrm{Q}}_\psi \tag{2.6}$$

where σ is the static stability parameter, $f_0$is the Coriolis parameter and ω is the vertical wind in pressure coordinates (Pa s^{-1}). The Q-vector is defined as:

$$\vec{\mathrm{Q}}_\psi = \left\{ \frac{-R}{P} \left(\frac{\partial \vec{V}_\psi}{\partial x} \cdot \nabla_{\mathrm{p}} T \right), \frac{-R}{P} \left(\frac{\partial \vec{V}_\psi}{\partial y} \cdot \nabla_{\mathrm{p}} T \right) \right\} \tag{2.7}$$

where all horizontal derivatives are taken on isobaric surfaces, R is the dry air gas constant, P is the pressure level (Pa), $\vec{V}_\psi$ is the vector nondivergent observed wind (m s^{-1}), and T is the temperature (K). The units of $\vec{\mathrm{Q}}_\psi$ are K $m^{-1}s^{-1}$. The generalized Q-vector may be interpreted as the vector rate of change of the horizontal temperature gradient following the motion of a fluid particle moving along a trajectory defined by the non-divergent observed wind. Alternately, the *Q*-vector reflects the lower branch of the secondary ageostrophic circulation and points toward regions of rising motion (Hoskins and Pedder 1980). To the extent that the right hand side (RHS) of the omega equation can be assumed to be sinusoidal, the left hand side (LHS) is commonly approximated as

$$-\omega \propto w \propto -2\nabla_{\mathrm{p}} \cdot \vec{\mathrm{Q}}_\psi \tag{2.8}$$

which implies that convergent *Q* vectors can be associated with rising motion. While this approximation helps to provide context, an accurate representation of synoptic-scale vertical motions requires solving for omega from the AB omega equation (Clough et al. 1996). Before proceeding with this calculation, it is useful to consider the meaning of the individual terms on the LHS of the AB omega equation:

$$\underbrace{\sigma\nabla_{\mathrm{p}}{}^2\omega}_{\boldsymbol{A}} + \underbrace{f_0\frac{\partial^2}{\partial \mathrm{p}^2}\omega}_{\boldsymbol{B}} = RHS \tag{2.9}$$

When integrated with appropriate lateral and vertical boundary conditions, the first term (**A**) represents the horizontal coupling and the second term (**B**) provides vertical coupling of $\nabla_p \cdot \vec{Q}$ at different levels and locations. Consequently, it is important to consider the full three-dimensional field of the RHS in order to properly resolve the magnitude and sign of the vertical motions for a specific location. Expanding on earlier work by Durran and Snellman (1987) and using the electrostatic concept of action at a distance, Clough et al. (1996) examined the impact of point, dipole, and quadra-pole spherical distributions of $\nabla_p \cdot \vec{Q}$ as a function of their vertical location, latitude, and surrounding stability. It was demonstrated that increasing latitude or static stability confines the vertical and horizontal influence of $\nabla_p \cdot \vec{Q}$. The influence of multiple sources of $\nabla_p \cdot \vec{Q}$, especially positive-negative dipoles, localizes omega and confines it to a spatial pattern similar to that of $\nabla_p \cdot \vec{Q}$ (which supports the sinusoidal approximation mentioned above). Durran and Snellman (1987) showed earlier that longer wavelength features within the distribution of $\nabla_p \cdot \vec{Q}$ dominate, which leads to smoother appearing omega fields compared to the RHS term. Hence, small-scale $\nabla_p \cdot \vec{Q}$ features in the reanalyses resulting from poorly resolved terrain-induced or convective processes will tend to be less apparent in the final omega field relative to synoptic-scale features. The case study in Chapter 3 will support these statements.

Since the postprocessing of the reanalysis reduces the horizontal resolution to ~ 160 km, the horizontal gradients in wind and temperature, the convergence of the Q vector, and the magnitude of the derived vertical motions in this study are reduced as well. Elbern et al. (1998) showed that a mesoscale model provided considerably larger

values of $\nabla_p \cdot \vec{Q}$ than those derived from coarse ECMWF analysis grids. About 70% of the difference in $\nabla_p \cdot \vec{Q}$ was attributable to reduced gradients of geostrophic wind with the remaining fraction due to reduced gradients of potential temperature. Hence, the magnitudes of synoptic-scale vertical motion derived from the postprocessed ERA-Interim reanalysis likely underestimate those that could be obtained from the original T255 grids.

The common method of successive over relaxation is used to solve the full three-dimensional omega equation (Stuart 1967). Homogeneous zero boundary conditions are used for both lateral and vertical boundaries except in the case study presented in Chapter 3 where the impacts of the vertical boundary conditions are documented. Vertical motions resulting from poorly-resolved mountain flows are eliminated by setting the bottom boundary to zero, which also helps to filter other mesoscale vertical motions.

Statistical Methods

The climatological distribution of synoptic-scale ascent, as calculated by the alternative balance omega equation, is established by an accumulation method. Employing an Eulerian perspective, the climatological mean ascent at each grid point is given by

$$\bar{\omega} = \frac{1}{n}\sum_{i=1}^{n} \beta_i \omega_i^m \tag{2.10}$$

where the summation is taken over the n six-hour observations in the data set and ω^m is the grid point vertical column maximum ascent (minimum omega) which may occur on any of the five isobaric surfaces employed in the calculation of omega. β is an event parameter which takes on the value of 1 when ω^m is less than -0.075 Pa s^{-1} (recall ascending motions are negative in pressure coordinates) and 0 for all other eventualities. The use of this event parameter excludes descending motions and minor ascending motions from climatological statistics. The threshold value was developed by subjective evaluation of preliminary results in this specific data set. As discussed in the previous section, values of omega depend on model resolution which renders direct comparison of the present threshold to those employed in other studies difficult.

The climatological mean ascent can subsequently be decomposed into two independent parts, (1) the climatological mean ascent frequency (percentage of the time a grid point exceeds the threshold value)

$$f = \frac{1}{n}\sum_{i=1}^{n}\beta_i \times 100 \tag{2.11}$$

and, (2) the climatological mean ascent magnitude at each grid point

$$\overline{\omega^*} = \frac{1}{\sum_{i=1}^{n}\beta_i}\sum_{i=1}^{n}\beta_i\omega_i^m \tag{2.12}$$

Collectively these three metrics are used in this study to represent the statistical prevalence and local intensity of ascent, and thus storms, over the 19 cool seasons

(October-April). This approach is scalable for any sample size spanning single synoptic events, months, or years.

Standardized anomalies of mean ascent are calculated for each of the 19 cool seasons, at each grid point, by removing the climatological mean ascent and dividing by the standard deviation. Month to month variations are examined in a similar fashion. Subsequently, interannual variations in cool season standardized anomalies are examined by principal component analysis (PCA) based on the correlations between all pairs of spatial maps. This analysis results in principal components, which are spatial maps of standardized anomalies in ascent, and eigenvectors which are time series (Horel 1984). The principal components are obtained by projecting the initial set of seasonal anomalies onto the vector space defined by the eigenvectors of the 19 x 19 correlation matrix. For simplicity, the eigenvectors will hence forth be referred to as the principal component time-series. The eigenvalues, associated with each respective eigenvector, are scaled by the total units of variance (19 in this case) and thus represent the percentage of variance explained by each eigenvector, or principal component time series. Correlations between the principal component time-series and the time series of known modes of interannual climate variability as well as seasonal precipitation anomaly time series help to assess to what extent the principal components represent physical processes. A significant limitation for this part of the study is the limited sample of 19 cool seasons available from the ERA-interim reanalysis.

CHAPTER 3

CALCULATING VERTICAL MOTION: AN EXAMPLE CASE

The purpose of this chapter is to illustrate the method for calculating vertical motion during a strong synoptic disturbance that traversed the western US on 15-16 April 2002. The structure and evolution of this system, dubbed the 'Tax Day Storm', was examined in detail by West and Steenburgh (2010; hereafter WS10). For clarity, all the figures presented in this chapter are centered on the western United States, even though the calculations were completed for the entire grid introduced in the previous chapter.

Figure 3.1 demonstrates the process for computing the non-divergent component of the ERA-interim analyzed wind at a time of strong ascent associated with the tax day storm. Following the removal of the zonal and meridional mean wind from the entire domain, the relative vorticity is calculated (Fig. 3.1a). As shown in Fig. 3.1b, the stream function, ψ, is then calculated from the relative vorticity field and the non-divergent components of the wind derived from the gradients in ψ.

The approach used to diagnose ascent, described in Chapter 2, is best illustrated by examining cross sections along the transect W-E in Figure 3.1a as the Tax Day Storm evolves (Figs. 3.2-3.7)**.** The top panel in each figure shows the ERA-interim vertical motion field on the post-processed grid while the bottom panel shows the vertical motion

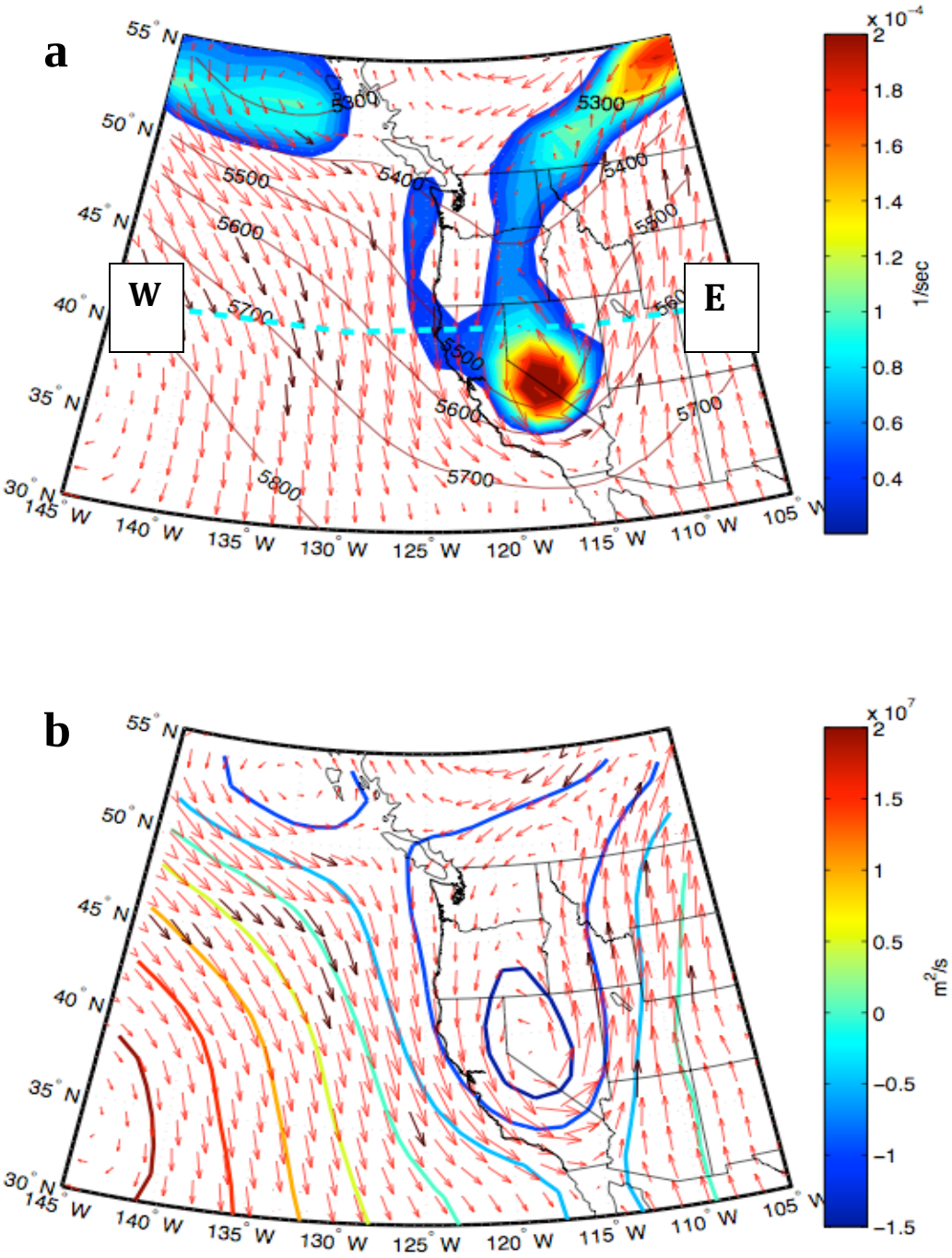

Figure 3.1. Example of the non-divergent wind calculation for 18 UTC 15 Apr. 2002. (a) Observed wind with the areal mean removed (vectors), geopotential height at 500 hPa surface (labeled contours in decameters), and relative vorticity (shaded). The dashed cyan line from W-E is the location of the cross sections shown in subsequent figures. (b) Non-divergent wind (vectors) and the stream function (colored contours). The dark colored vectors are for scale, representing wind magnitude of 20 ms $^{-1}$.

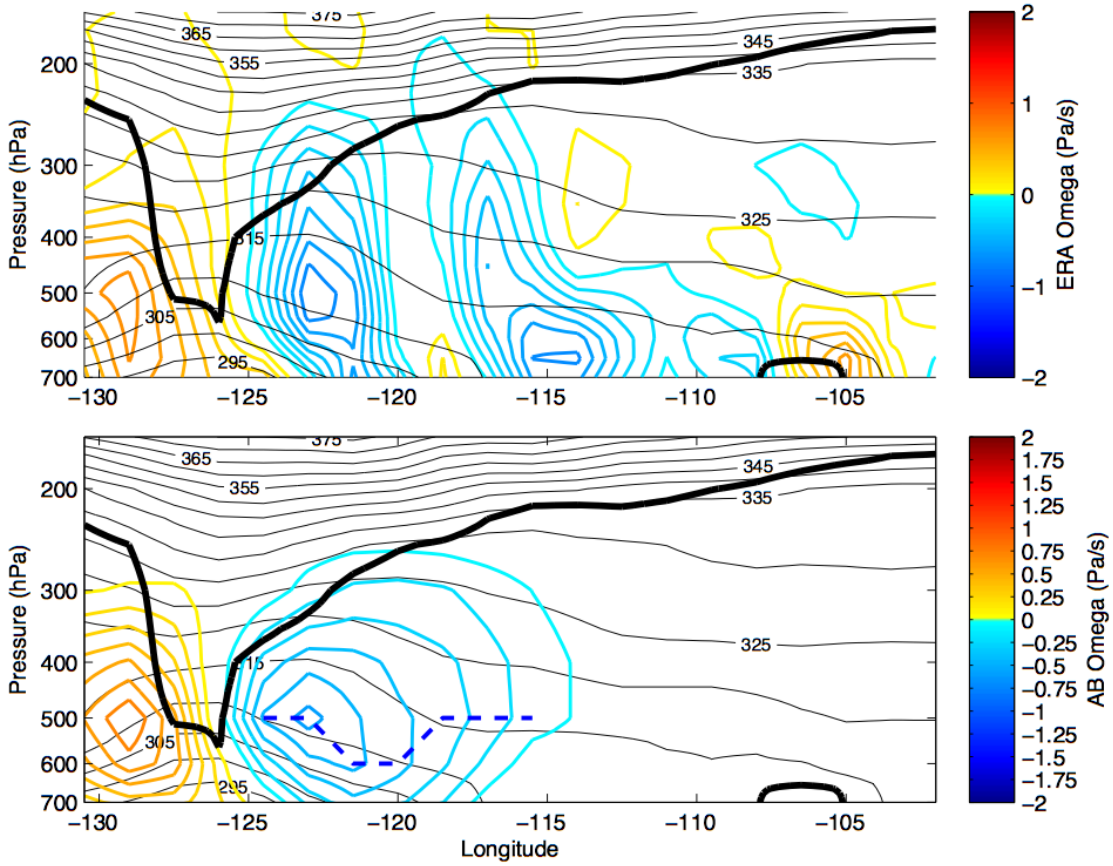

Figure 3.2. Cross section along W-E (Fig 3.1) for 06 UTC 15 Apr. Comparison between ERA-interim omega (top panel) and AB omega (lower panel). Cool (warm) colored contours represent ascending (descending) motion. The dashed blue line (lower panel) represents the column maximum ascent values that are retained for statistical analysis for this time step. In both panels, the heavy black line is the 2 PVU dynamic tropopause surface and thin black contours are potential temperature (K).

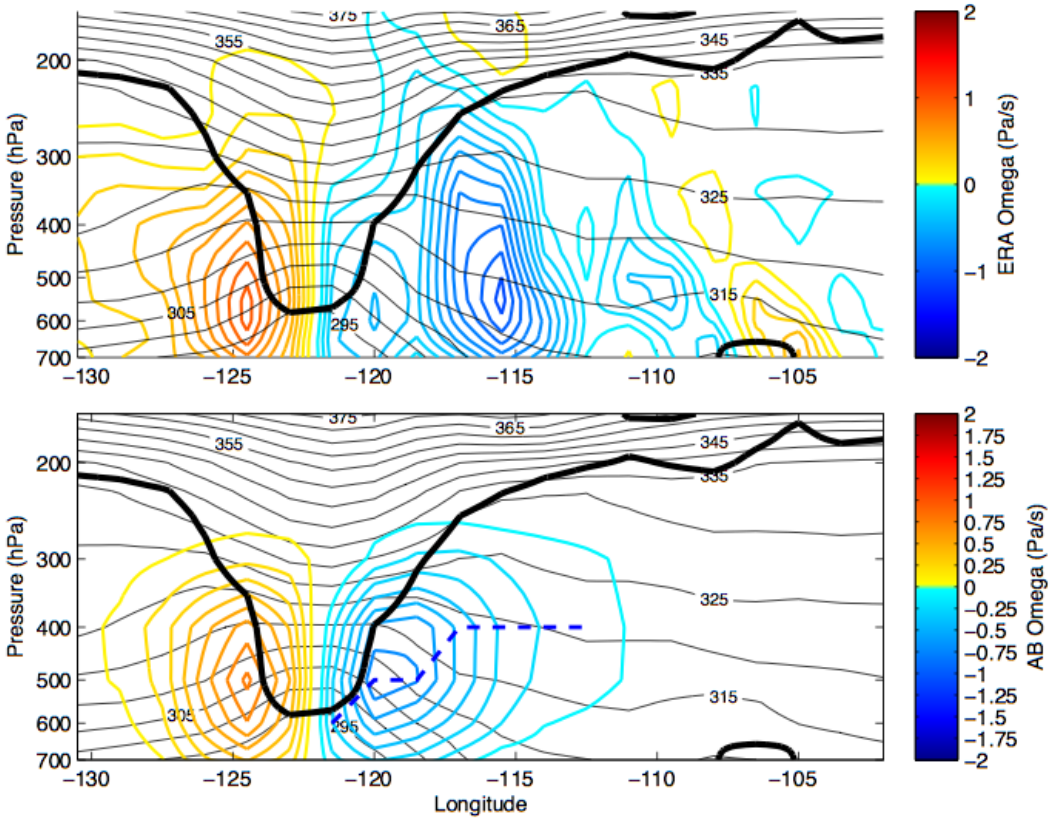

Figure 3.3. Cross section along W-E (Fig 3.1) for 12 UTC 15 Apr. Comparison between ERA-interim omega (top panel) and AB omega (lower panel). Cool (warm) colored contours represent ascending (descending) motion. The dashed blue line (lower panel) represents the column maximum ascent values that are retained for statistical analysis for this time step. In both panels, the heavy black line is the 2 PVU dynamic tropopause surface and thin black contours are potential temperature (K).

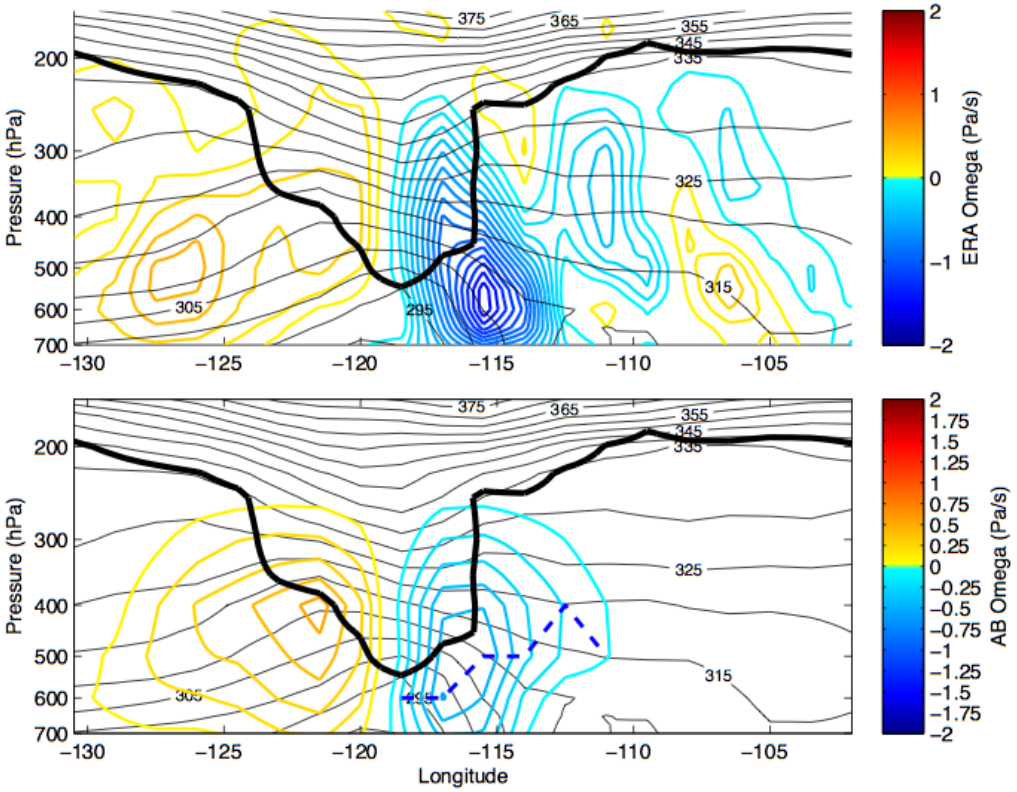

Figure 3.4. Cross section along W-E (Fig 3.1) for 18 UTC 15 Apr. Comparison between ERA-interim omega (top panel) and AB omega (lower panel). Cool (warm) colored contours represent ascending (descending) motion. The dashed blue line (lower panel) represents the column maximum ascent values that are retained for statistical analysis for this time step. In both panels, the heavy black line is the 2 PVU dynamic tropopause surface and thin black contours are potential temperature (K).

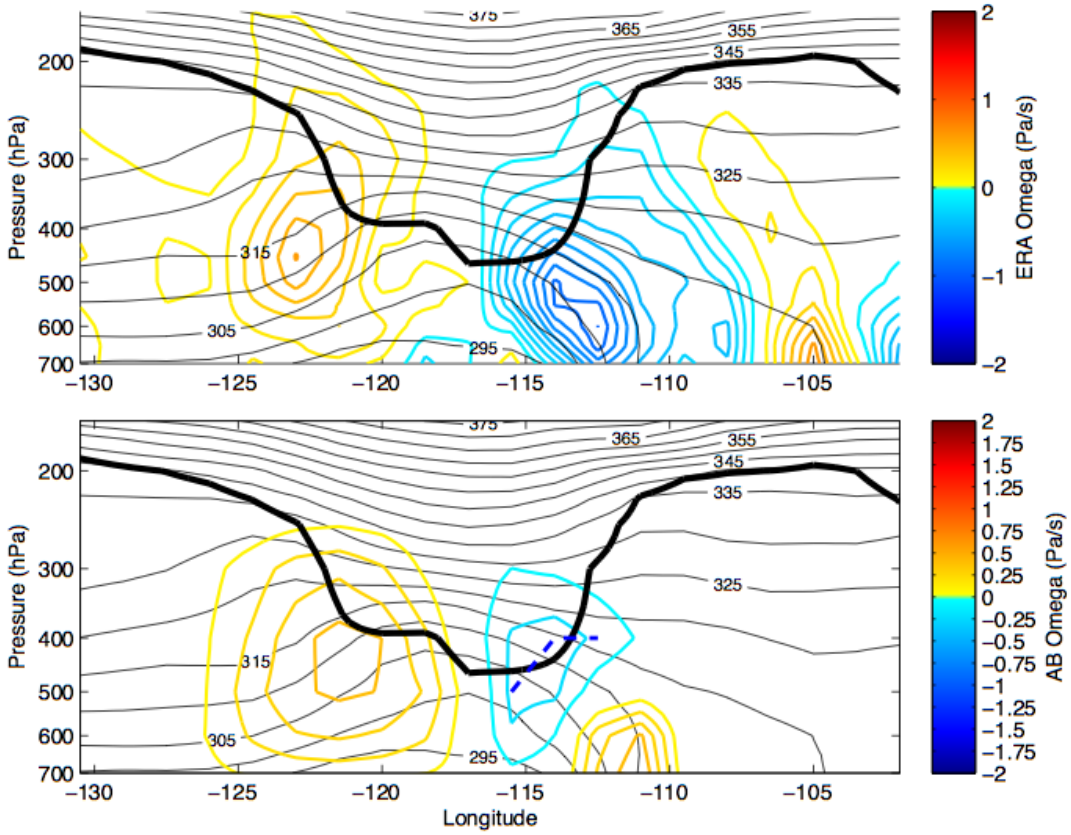

Figure 3.5. Cross section along W-E (Fig 3.1) for 00 UTC 16 Apr. Comparison between ERA-interim omega (top panel) and AB omega (lower panel). Cool (warm) colored contours represent ascending (descending) motion. The dashed blue line (lower panel) represents the column maximum ascent values that are retained for statistical analysis for this time step. In both panels, the heavy black line is the 2 PVU dynamic tropopause surface and thin black contours are potential temperature (K).

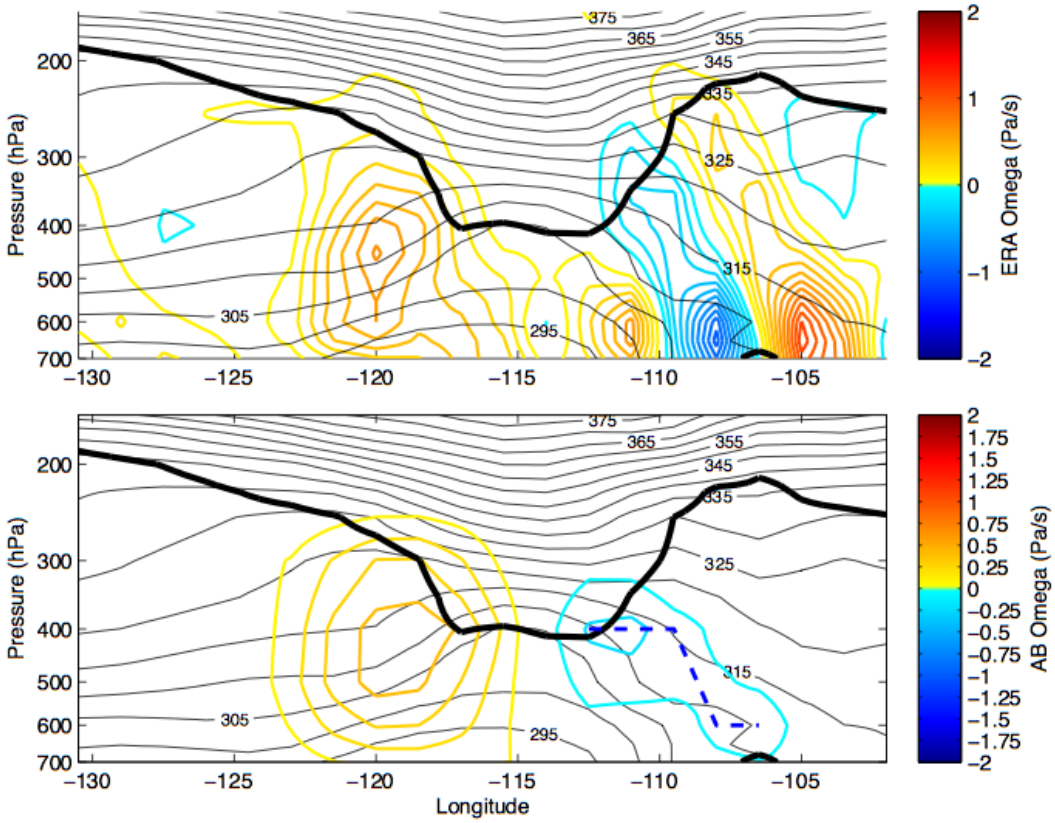

Figure 3.6. Cross section along W-E (Fig 3.1) for 06 UTC 16 Apr. Comparison between ERA-interim omega (top panel) and AB omega (lower panel). Cool (warm) colored contours represent ascending (descending) motion. The dashed blue line (lower panel) represents the column maximum ascent values that are retained for statistical analysis for this time step. In both panels, the heavy black line is the 2 PVU dynamic tropopause surface and thin black contours are potential temperature (K).

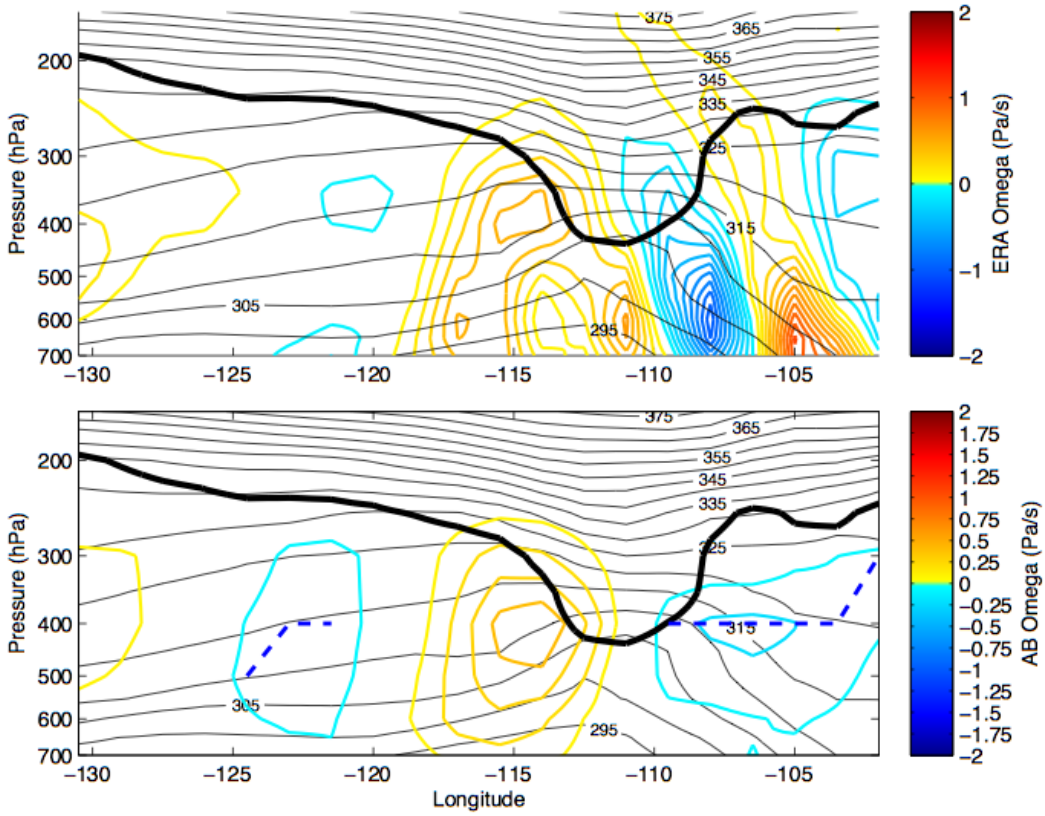

Figure 3.7. Cross section along W-E (Fig 3.1) for 12 UTC 16 Apr. Comparison between ERA-interim omega (top panel) and AB omega (lower panel). Cool (warm) colored contours represent ascending (descending) motion. The dashed blue line (lower panel) represents the column maximum ascent values that are retained for statistical analysis for this time step. In both panels, the heavy black line is the 2 PVU dynamic tropopause surface and thin black contours are potential temperature (K).

obtained by solving the AB omega equation. Common to each panel is the dynamic tropopause (2 PVU) surface and distribution of potential temperature while the dashed lines in the lower panels indicate the level of maximum ascent for gridpoints where the derived omega is less than -0.075 Pa/sec at one or more levels.

Evident in Figs. 3.2-3.7, the Tax Day Storm was associated with a significant tropopause disturbance progressing from west to east through the cross-section. Not as clearly illustrated, near-surface frontogenesis took place during the later stages of the storm (WS10). Throughout the event, vertical motions derived from the AB omega equation exhibit a smoother distribution than the post-processed omega from the ERA-interim and tend to be more closely associated with the tropopause disturbance and attendant gradients in potential temperature. This is particularly apparent in Fig. 3.2 where the ERA-interim shows rising motions downstream and well removed from the tropopause depression that are likely related to mountain-flow interactions and/or convective processes. The AB omega at this time shows only a strong dipole of sinking and rising motion situated symmetrically about the tropopause depression. Additionally, throughout these cross sections the model topography impinges on the 700 hPa surface near 106° W, which is typically marked by an interior PV anomaly (solid black line in near bottom of Figs. 3.2,3.3,3.6) and an orographically forced couplet of up- and down-drafts (Figs. 3.2-3.7 top panel). The absence of such motions in the AB omega field is an example of the dynamic filtering that occurs due to the scale selection and zero boundary conditions of the AB omega equation. This filtering is considered appropriate as we are interested in the motions directly associated synoptic-scale transients and not orographic or other mesoscale-induced motions.

The magnitude of the ERA-interim omega tends to be larger than that derived from the AB omega equation, especially where heavy precipitation and strong latent heat release are evident in both observations and in the ERA-interim reanalysis (Figs. 3.4, 3.5). Since ascent arising from convective processes is intentionally attempted to be filtered, the ascent derived from the AB omega equation assumes dry static stability, which is an overestimate of the stability when the atmosphere is saturated. As discussed in the previous chapter, higher stability implies weaker derived vertical motions. Additional reductions in the magnitude of omega are likely a consequence of the coarse resolution of the post-processed data as compared to native ERA-interim resolution.

Further insight into the role of stability, the number of vertical layers included in the integration, and the impact of lower boundary conditions on the solution to the AB omega equation is provided in Figs 3.8-3.9**.** The top panel in each figure shows the RHS of the AB omega equation, while the subsequent panels show the derived omega computed with different assumptions. As discussed in Chapter 2, $\nabla_p \cdot \overrightarrow{Q}$ tends to have finer-scale structures than the derived omega fields. The impact of static stability is quite evident, since the magnitudes of the derived omega fields are greatly reduced in the stratosphere as a result of high static stability and increased somewhat in tropospheric regions of weak static stability compared to the corresponding magnitudes of $\nabla_p \cdot \vec{Q}$ in those respective regions. Solving the omega equation using only 5 vertical layers, as employed in the next chapter, instead of all 31 levels does not substantively change the distribution of derived vertical motion (compare the b and c panels in Figs. 3.8, 3.9). Similarly, minor differences are apparent if the 5-layer solution uses lower boundary conditions prescribed by the ERA-interim 700 hPa omega compared to setting

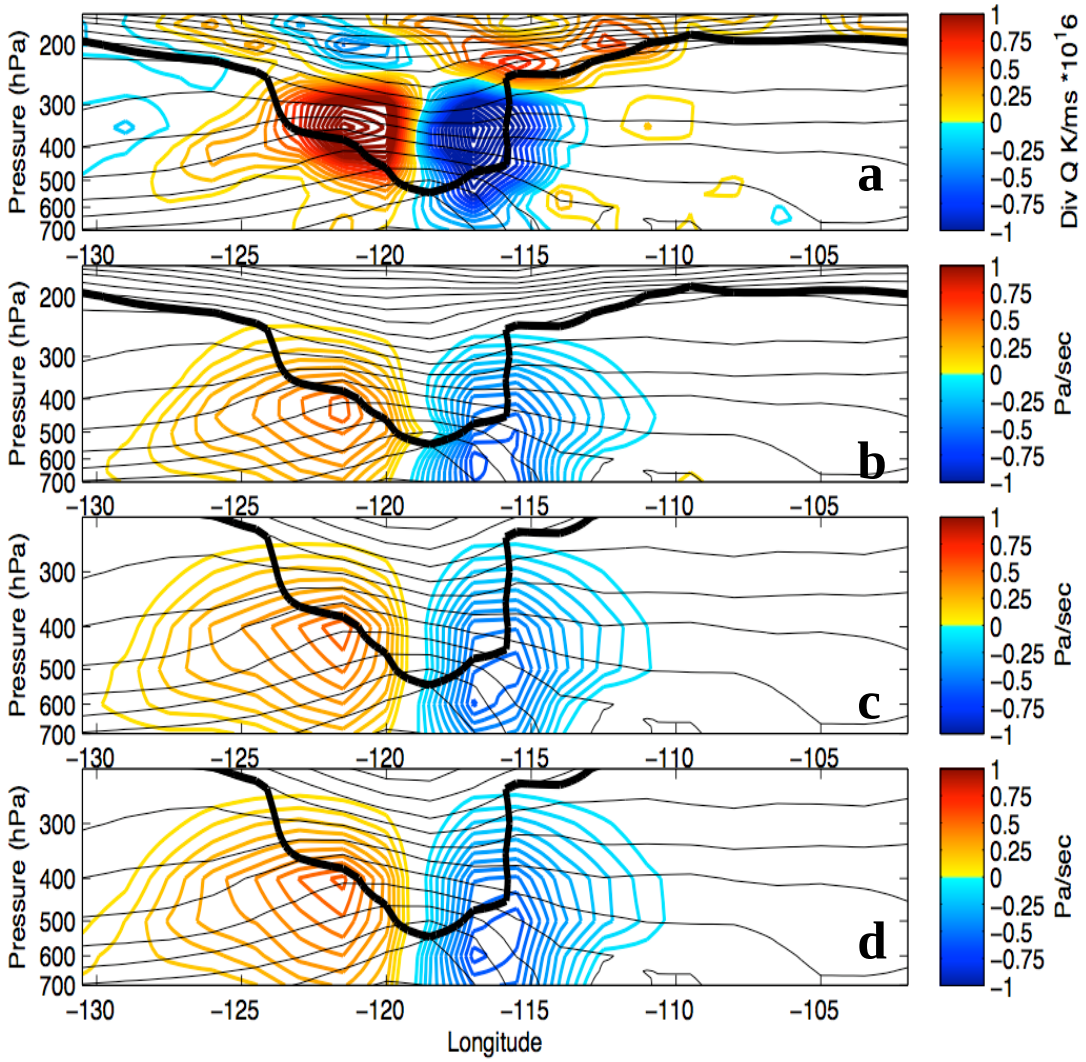

Figure 3.8. Comparison of integration techniques for 18 UTC 15 April 2002. (a) -2 $\nabla_p \cdot \vec{Q}$ (K m^{-2} s^{-1}). (b) Alternative Balance (AB) omega solution using 31 vertical pressure levels and zero boundary conditions. (c) AB omega solution using 5 pressure levels (300, 400, 500, 600, 700 hPa). (d) AB omega solution using 5 pressure levels and lower boundary conditions (700 hPa) prescribed from the ERA-interim omega. Common to all panels: 2 PVU dynamic tropopause surface (heavy black contour) potential temperature (thin black contours).

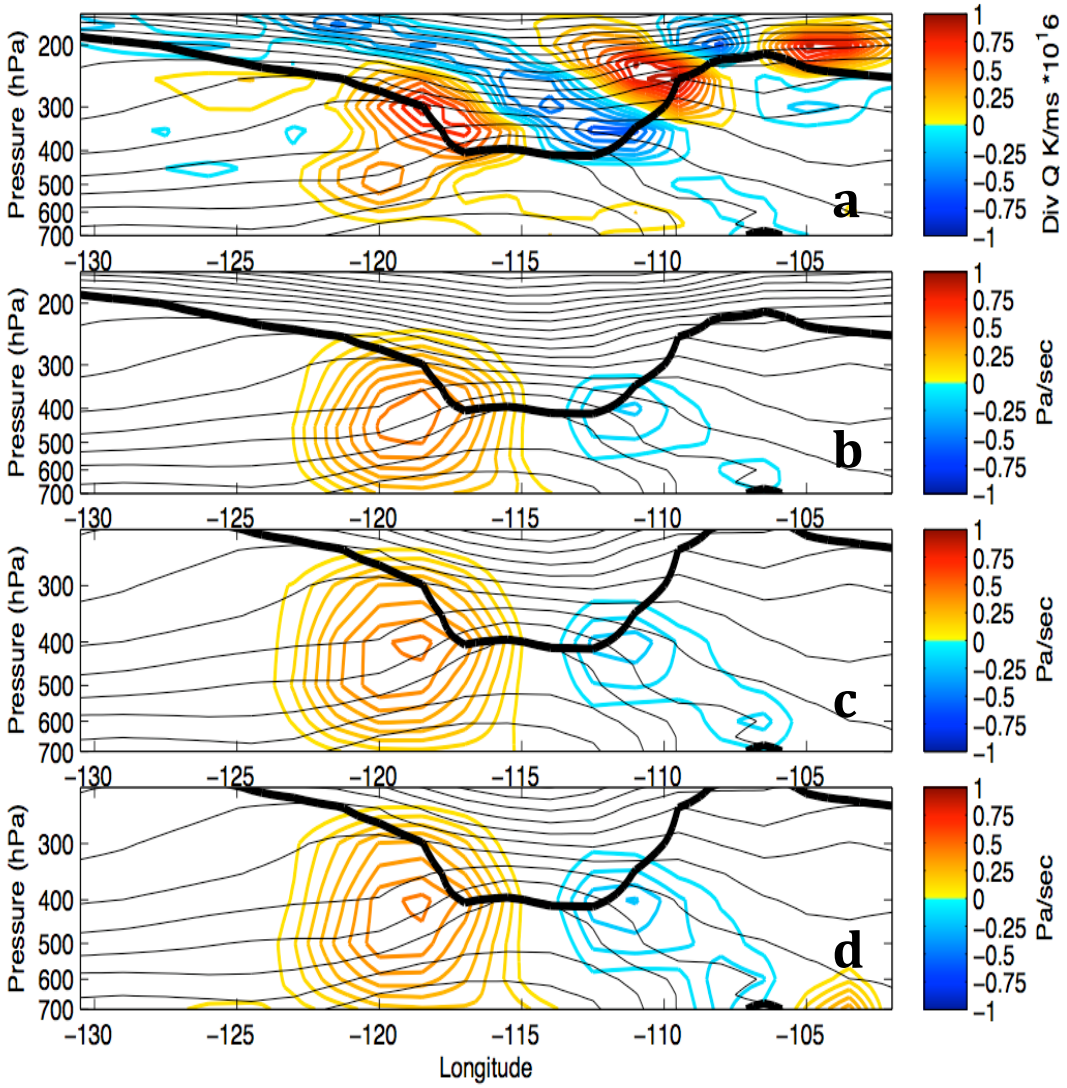

Figure 3.9. Comparison of integration techniques for 06 UTC 16 April 2002. (a) -2 $\nabla_p \cdot \vec{Q}$ (K m^{-2} s^{-1}). (b) Alternative Balance (AB) omega solution using 31 vertical pressure levels and zero boundary conditions. (c) AB omega solution using 5 pressure levels (300, 400, 500, 600, 700 hPa). (d) AB omega solution using 5 pressure levels and lower boundary conditions (700 hPa) prescribed from the ERA-interim omega. Common to all panels: 2 PVU dynamic tropopause surface (heavy black contour) potential temperature (thin black contours).

the lower boundary condition to be zero (compare the c and d panels). Hence, all subsequent results employ zero lower boundary conditions and 5 pressure levels for computational efficiency (shown in panels Figs. 3.8c, 3.9c).

Figures 3.10-3.15 provide a plan view perspective on the evolution of the column maximum AB derived ascent and descent at six hour time steps from 06 UTC 15 - 06 UTC 16 April 2002 relative to radar reflectivity and infrared satellite imagery. The column maximum ascent (descent) at each grid point may be occurring on any of the 5 isobaric surface employed in the calculation. Where both ascent and descent occur within the same column, the value of ascent is displayed. A light blue line encircles regions within which the event parameter, described in Chapter 2, is set to one, and thus denotes the 'storm footprint' at that point in time. Through the early phases of the Tax Day Storm, a quasi-symmetric dipole of rising and sinking motions is found centered about the 500 hPa trough axis (Figs. 3.10-3.12). This dipole pattern breaks down later in the event, and vertical motions become less spatially coherent and predictable in their locations and intensity relative to the location of the mid-tropospheric trough axis. Beginning at 00 UTC 16 April (Fig. 3.13), upward motions become elongated in an arc and partially encircle a region of downward motion. Over the next 12 hours (Figs. 3.14-3.15), the areas of strongest vertical motion bifurcate into weaker and more localized centers. The symmetry in structure and magnitude across the trough axis is no longer evident as upstream of the trough a robust region of sinking motions can still be found despite the more dispersed downstream features.

The agreement between the distribution of clouds and precipitation and the location of rising motions tends to increase through this event. Initially at 06-12 UTC 15

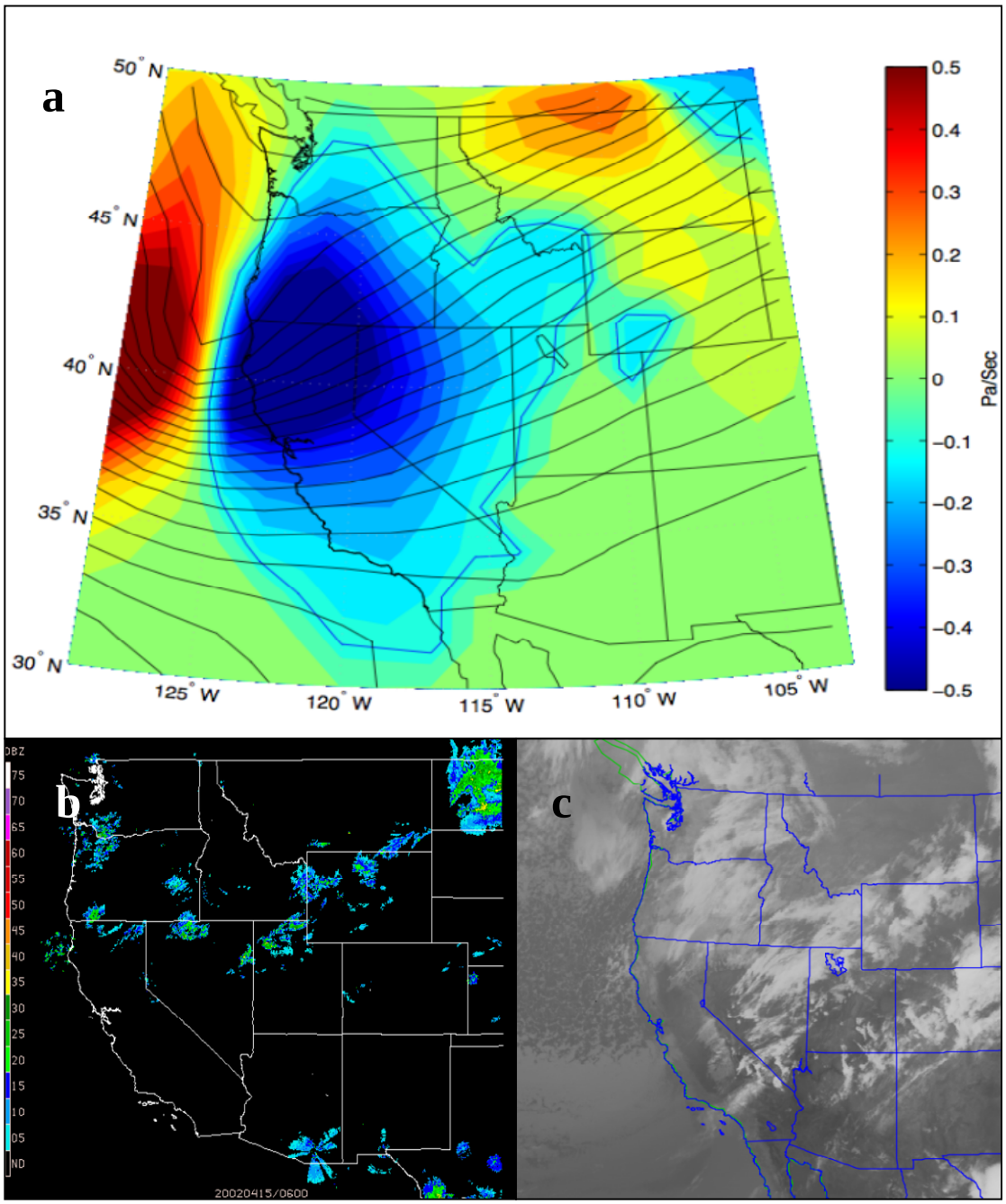

Figure 3.10. 06 UTC 15 April 2002. (a) Plan view representation of column maximum AB ascent (blue) and descent (red) and 500 hPa geopotential height (thin contours). Where both ascent and descent occur in the same column, ascent values are displayed. The thin blue line represents the -0.075 Pa s^{-1} threshold value defines the storm footprint. (b) Composite NEXRAD radar reflectivity. (c) Infrared satellite image (brightness temperature).

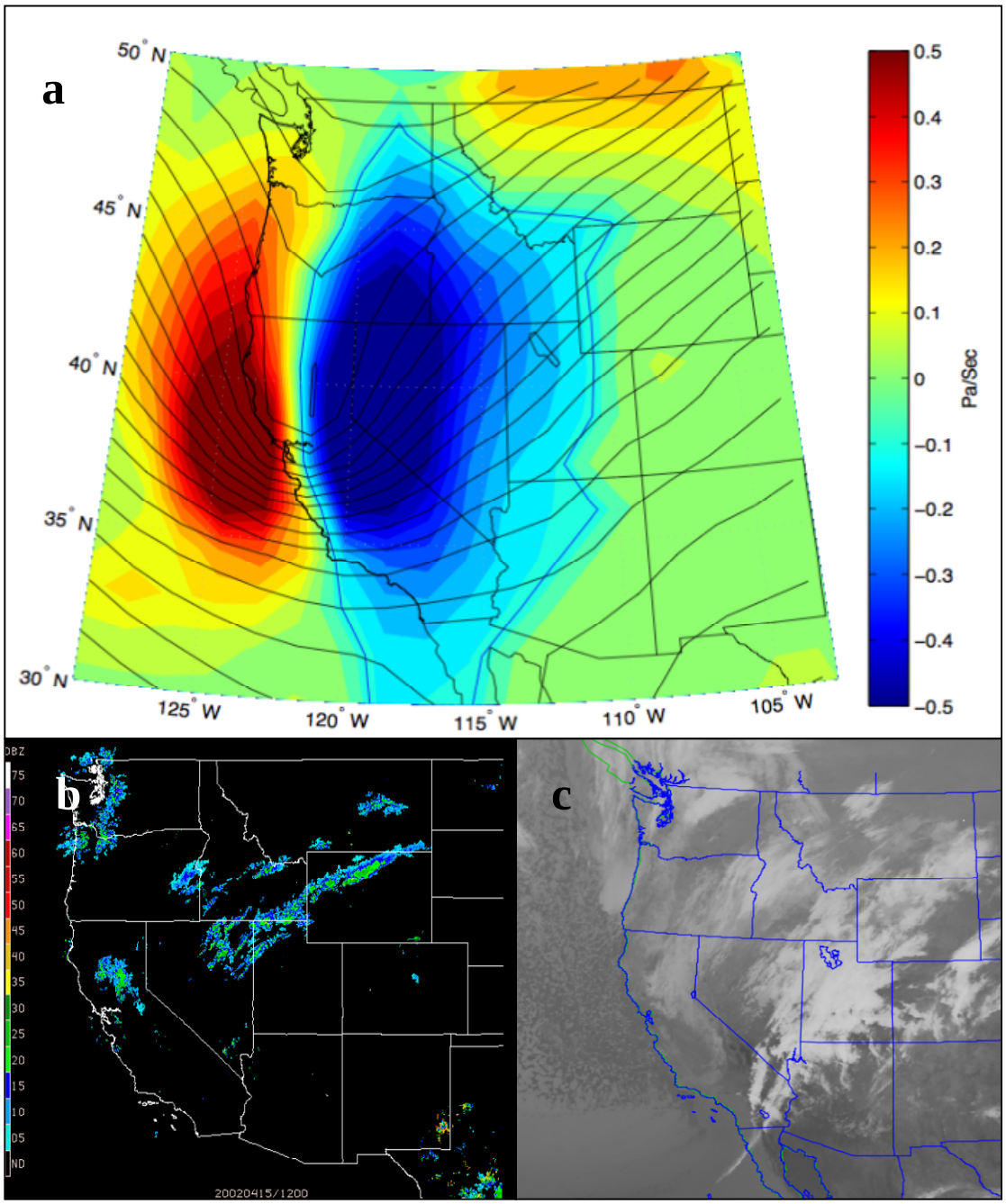

Figure 3.11. 12 UTC 15 April 2002. (a) Plan view representation of column maximum AB ascent (blue) and descent (red) and 500 hPa geopotential height (thin contours). Where both ascent and descent occur in the same column, ascent values are displayed. The thin blue line represents the -0.075 Pa s^{-1} threshold value defines the storm footprint. (b) Composite NEXRAD radar reflectivity. (c) Infrared satellite image (brightness temperature).

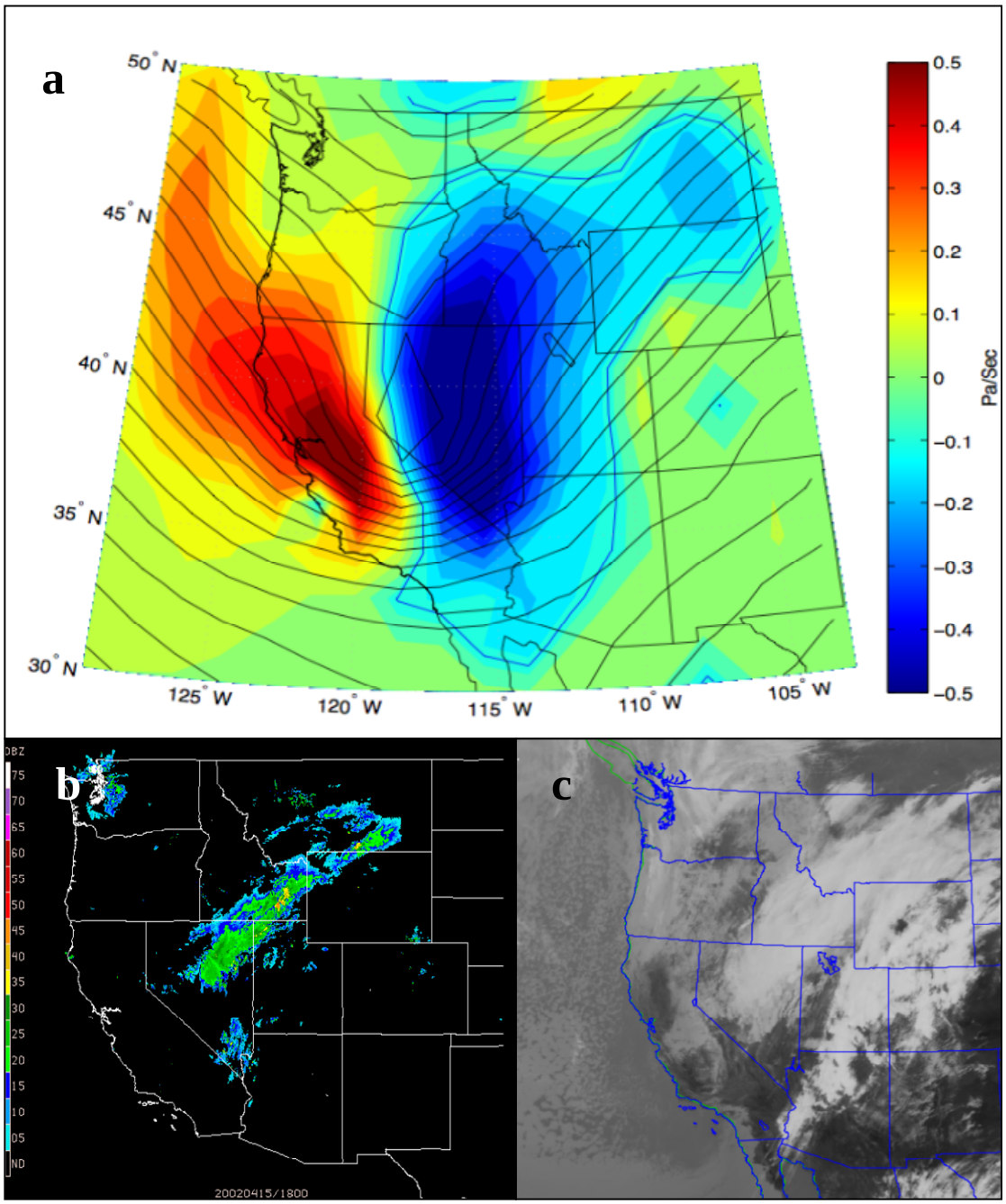

Figure 3.12. 18 UTC 15 April 2002. (a) Plan view representation of column maximum AB ascent (blue) and descent (red) and 500 hPa geopotential height (thin contours). Where both ascent and descent occur in the same column, ascent values are displayed. The thin blue line represents the -0.075 Pa s^{-1} threshold value defines the storm footprint. (b) Composite NEXRAD radar reflectivity. (c) Infrared satellite image (brightness temperature).

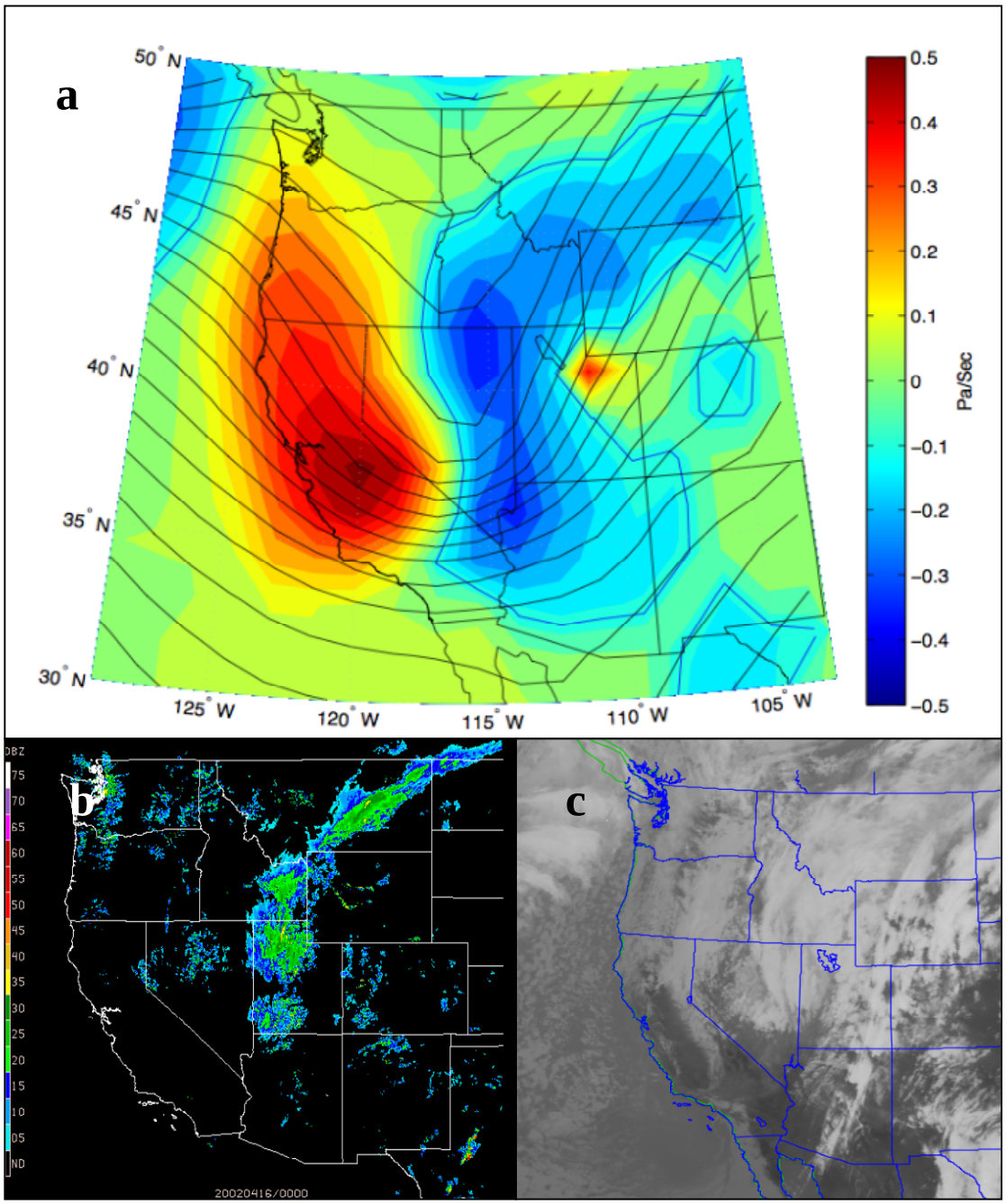

Figure 3.13. 00 UTC 16 April 2002. (a) Plan view representation of column maximum AB ascent (blue) and descent (red) and 500 hPa geopotential height (thin contours). Where both ascent and descent occur in the same column, ascent values are displayed. The thin blue line represents the -0.075 Pa s^{-1} threshold value defines the storm footprint. (b) Composite NEXRAD radar reflectivity. (c) Infrared satellite image (brightness temperature).

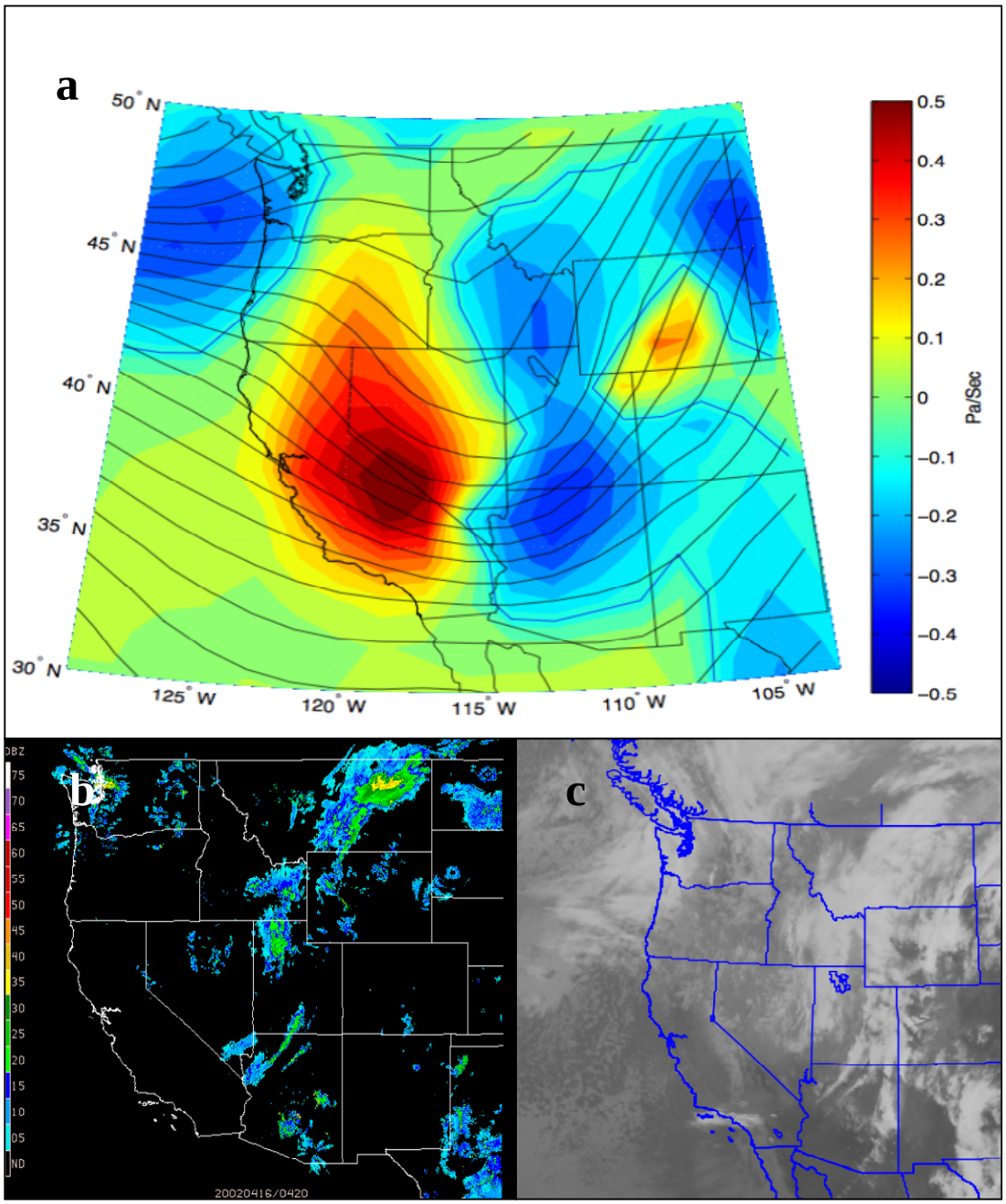

Figure 3.14. 06 UTC 16 April 2002. (a) Plan view representation of column maximum AB ascent (blue) and descent (red) and 500 hPa geopotential height (thin contours). Where both ascent and descent occur in the same column, ascent values are displayed. The thin blue line represents the -0.075 Pa s^{-1} threshold value defines the storm footprint. (b) Composite NEXRAD radar reflectivity from 0420 UTC to fill data gap. (c) Infrared satellite image (brightness temperature) from 04 UTC to fill data gap.

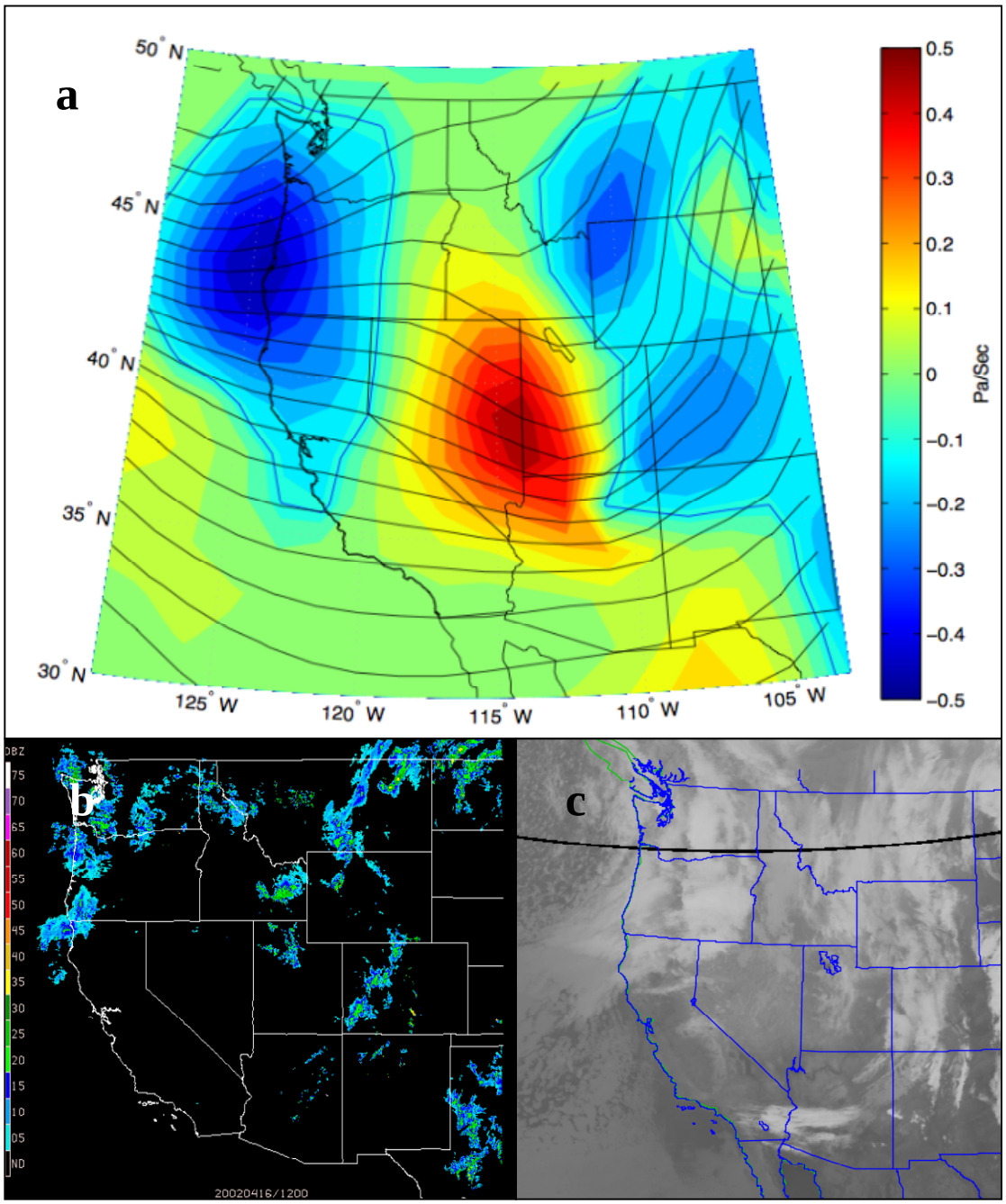

Figure 3.15. 12 UTC 16 April 2002. (a) Plan view representation of column maximum AB ascent (blue) and descent (red) and 500 hPa geopotential height (thin contours). Where both ascent and descent occur in the same column, ascent values are displayed. The thin blue line represents the -0.075 Pa s^{-1} threshold value defines the storm footprint. (b) Composite NEXRAD radar reflectivity. (c) Infrared satellite image (brightness temperature).

April (Figs 3.10-3.11), much of the strong synoptically driven rising motions are found in the cloud sparse air upstream of a region of clouds and precipitation in northern Utah and southern Idaho (analyzed by WS10 as an older frontal boundary). However, by 18 UTC 15 April (Fig 3.12), the distribution of ascent and the precipitation and cloud structures are in better agreement, as a new region of clouds and precipitation are generated in central Nevada and in an arc north through Idaho and Montana . This relationship persists until the rising motions weaken and precipitation becomes more dispersed at 12 UTC 16 April (Fig. 3.15).

The increasing relationship with time between precipitation and rising motion is likely a consequence of the timescales required to drive air first to saturation and then supersaturation. To elucidate this process, a simple scaling argument can be applied to a hypothetical parcel originating near the base of the trough. A parcel would need to ascend to roughly 600 hPa to achieve sufficient cooling to reach saturation if we assume a starting condition of 700 hPa, 0^0 C, and 50 % relative humidity. If we further assume that the parcel is being advected at a rate of 20 m s^{-1} through a region with ascent of -1 Pa s^{-1} (~ 0.1 m s^{-1}), the parcel would reach saturation in approximately 2-3 h and travel downstream ~200 km. Examining the location of the nascent cloud arc at 06 UTC 15 April (Figure 3.10), it is found to initiate approximately 200 km away from the trough axis along a streamline, which is roughly consistent with this simple scale analysis. Hence, while the cloud free air near the trough axis may seem inactive, it may actually be a vital preconditioning zone for air that will eventually be involved in precipitation processes. In the case of the tax day storm, rising motions intensify quickly as the approaching trough digs south and collapses in wavelength.

Figure 3.16 summarizes the mean ascent during the tax day storm. As described in Chapter 2, specifically equation 2.10, only maximum ascent with omega less than -0.075 Pa s^{-1} is accumulated from each time step, summed in this case over the 36 h period, and then divided by the 6 contributing time steps. The storm mean ascent suggests that the greatest vertical motion begins off the Oregon coast, intensifies across Nevada, and eventually extends across parts of Utah, Idaho, Wyoming and Montana. The splitting of maximum upward motion that begins at 00Z 16 April (Fig 3.13) is evident as well. Hence, this event would be described as having a storm track that begins along the west coast, reaches peak intensity over eastern Nevada, and then splits into two distinct tracks later on.

Animations of maximum ascent for every 6 h period during the 19 years were created and extensively examined to investigate other cases (not shown). The correspondence of the derived vertical motion with synoptic experience on the evolution of cool-season storms was quite apparent. Hence, it is reasonable to derive ascent statistics for any timescale of interest from individual cases to entire seasons, and this approach appears to represent a scalable approach to document storm tracks.

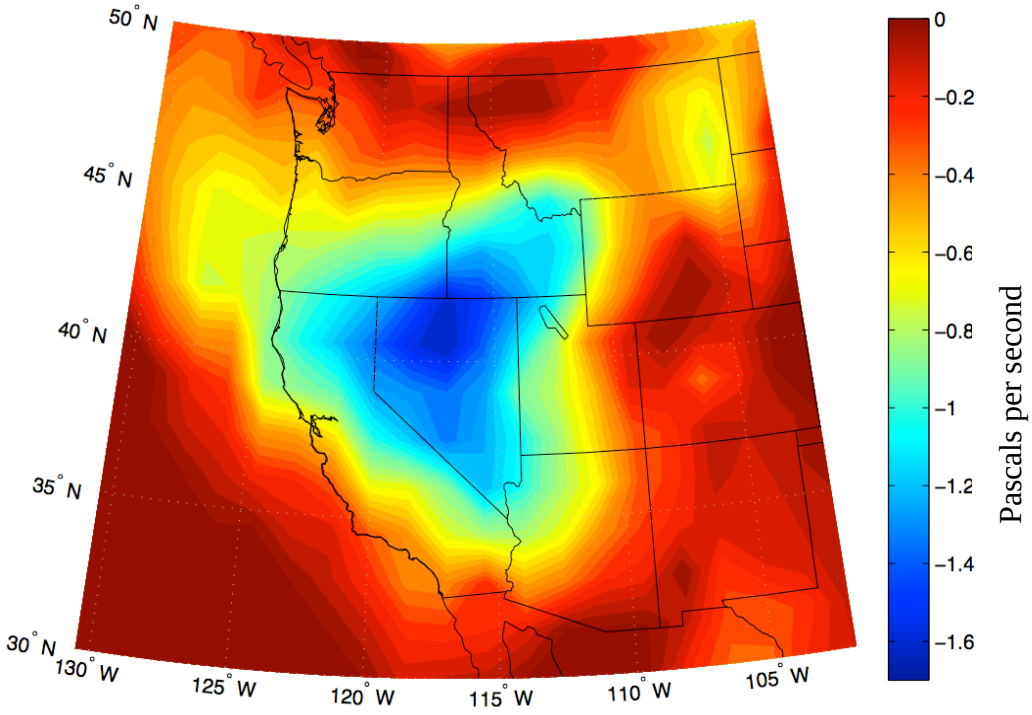

Figure 3.16. Tax Day Storm mean ascent (Pa s^{-1}).

CHAPTER 4

RESULTS

Climatological-Mean Synoptic-Scale Ascent

Summary statistics for the geographic distribution and variability in synoptically-forced ascent are presented in this chapter. The methods required to compute synoptic-scale ascent during each 6 h period within the 19 cool seasons (October 1989-April 2008) have been described in the previous two chapters. The climatological-mean ascent , defined by (2.10), is presented in Fig. 4.1a**.** A continuous belt of high mean ascent ($\overline{\omega}$ < -0.02Pa s^{-1}) is found in a roughly sinusoidal pattern across the domain and will be described here as defining the climatological mean storm track across the United States. Ascent is maximized in a broad region from the western edge of the domain northeastward to the British Columbia coast, where the first of three local maxima, labeled A in Fig. 4.1a, is encountered. Maximum A, with a value of $\overline{\omega}$ near -0.03 Pa s^{-1}, is located in a region well known for its frequent storminess and copious precipitation. The synoptic-scale ascent pathway then swings south in a narrow band along the western US coast before penetrating inland across Northern California. Mean ascent increases across southern Nevada and then reaches a second maximum, labeled B in Fig. 4.1a, over southern Arizona, which is one of the most arid regions of the nation. The apparent

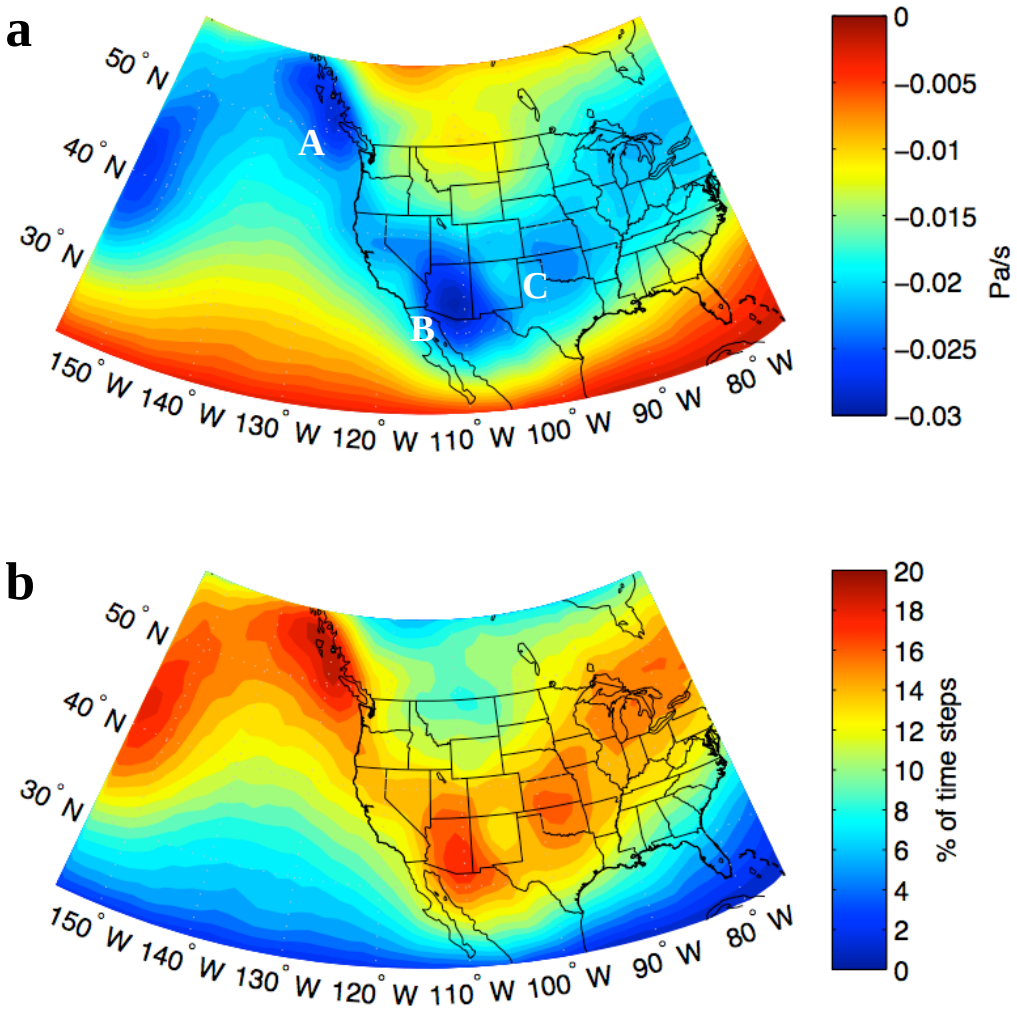

Figure 4.1. Climatological means for October 1989 – April 2008. (a) Mean synoptic-scale ascent (Pa s^{-1}) as defined by (2.10). White letters A-C denote local maxima in ascent. b.) Mean ascent frequency (percent of time steps) as defined by (2.11).

inconsistency between synoptic-scale ascent and limited precipitation in this region will be discussed in Chapter 5. The storm track, defined in terms of climatological-mean ascent, curves to the east-northeast splitting somewhat across New Mexico into portions of Texas and Colorado before reaching a third weaker maximum, labeled C in Fig. 4.1a, over Oklahoma. As will be discussed further in Chapter 5, this third maximum is found slightly east of the eastern Colorado surface cyclone maximum. From central Oklahoma, the primary ascent pathway continues northeast to the Great Lakes region. The lowest values of climatological mean synoptic-scale ascent within the mid-latitudes are found over the upper Missouri River basin.

The climatological mean frequency of ascent, f (2.11), shown in Fig. 4.1b, provides a nearly identical spatial perspective regarding synoptic-scale ascent as shown in Fig. 4.1a. Regions along the climatological-mean storm track experience synoptic-scale ascent greater than the threshold roughly 13% of the time (or once every 7.5 days) with local maxima experiencing ascent approaching 20 % of the time.

Also apparent in both the mean ascent and frequency metrics is a much weaker secondary storm track that stretches zonally across the Canadian Rockies in southern British Columbia, east across the high plains to Lake Winnipeg, and then rejoins the primary storm track in the Great Lakes Region. This feature, which is likely associated with Alberta clipper storms, will be discussed further in the next chapter.

A different perspective on synoptic-scale ascent is provided by Fig. 4.2, which shows the climatological mean ascent magnitude, defined by (2.12) to be the total accumulated ascent at each grid point divided by the number of 6 h periods when the ascent is greater than the specified threshold at each grid point. This metric simply

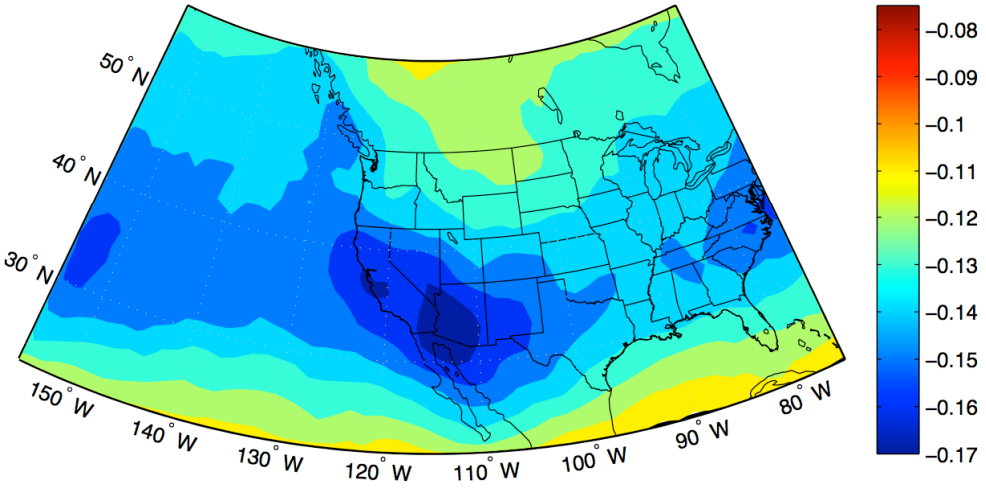

Figure 4.2. Climatological mean ascent intensity (Pa s^{-1}) as defined by (2.12).

defines the average maximum ascent independent of the number of times it actually takes place. For example, storms that reach 35^{o}N, 135^{o}W tend to have strong rising motion when they occur (Fig. 4.2) but, since they do not happen as often (Fig. 4.1b), the climatological mean ascent in this area is relatively low (Fig. 4.1a). Of particular interest is that ascent over Arizona (northeastern Montana) occurs fairly frequently (infrequently) and the intensity of that ascent is high (low).

Seasonality of Synoptic-Scale Ascent

The climatological seasonal cycle of synoptic-scale ascent is presented in Figs. 4.3-4.5. The climatological monthly mean ascent ((2.10) with the sample limited to time steps in a given month) is shown in Fig. 4.3 while each month's contribution to the climatological cool-season's accumulated ascent (Oct-Apr) is shown in Fig. 4.4. For formatting convenience, the panels for October are omitted from those figures. The month-to-month change in climatological monthly mean ascent is shown in Fig. 4.5, which highlights intraseasonal shifts in the location and magnitude of the storm tracks. Collectively, these three metrics show that regions of strong ascent migrate southward through February before advancing north again during March and April, which is consistent with the seasonal progression of mean upper-tropospheric ridging over the western North America. For the domain as a whole, December storms contribute the largest amount of ascent of any particular month, ascent tends to diminish in January, and February exhibits a more zonal storm track as compared to other months.

Embedded within these broad trends are important regional and intra-seasonal variations. Relative to October, mean ascent increases in most regions during November

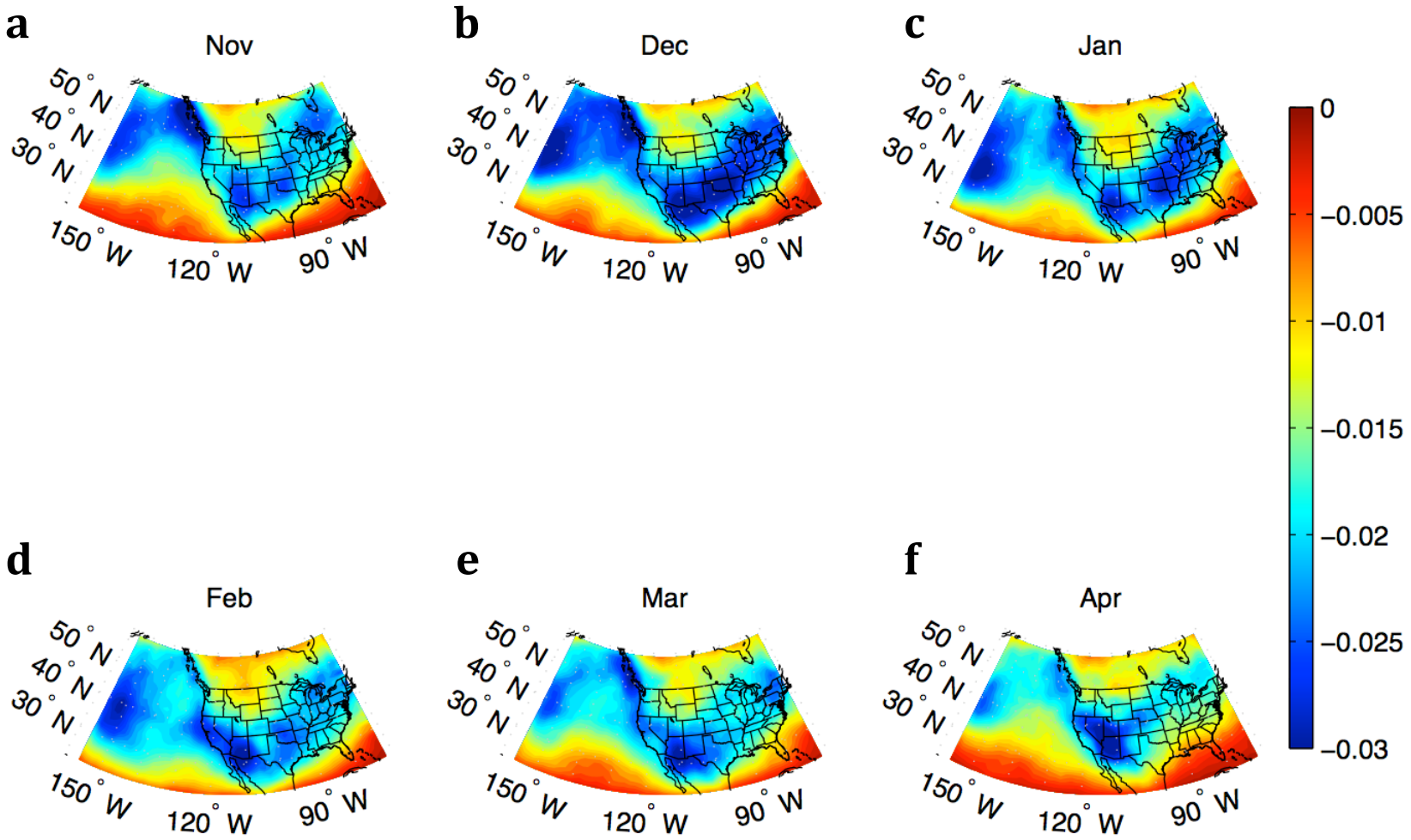

Figure 4.3. Climatological mean ascent (Pa s^{-1}) for each month November (a)-April (f).

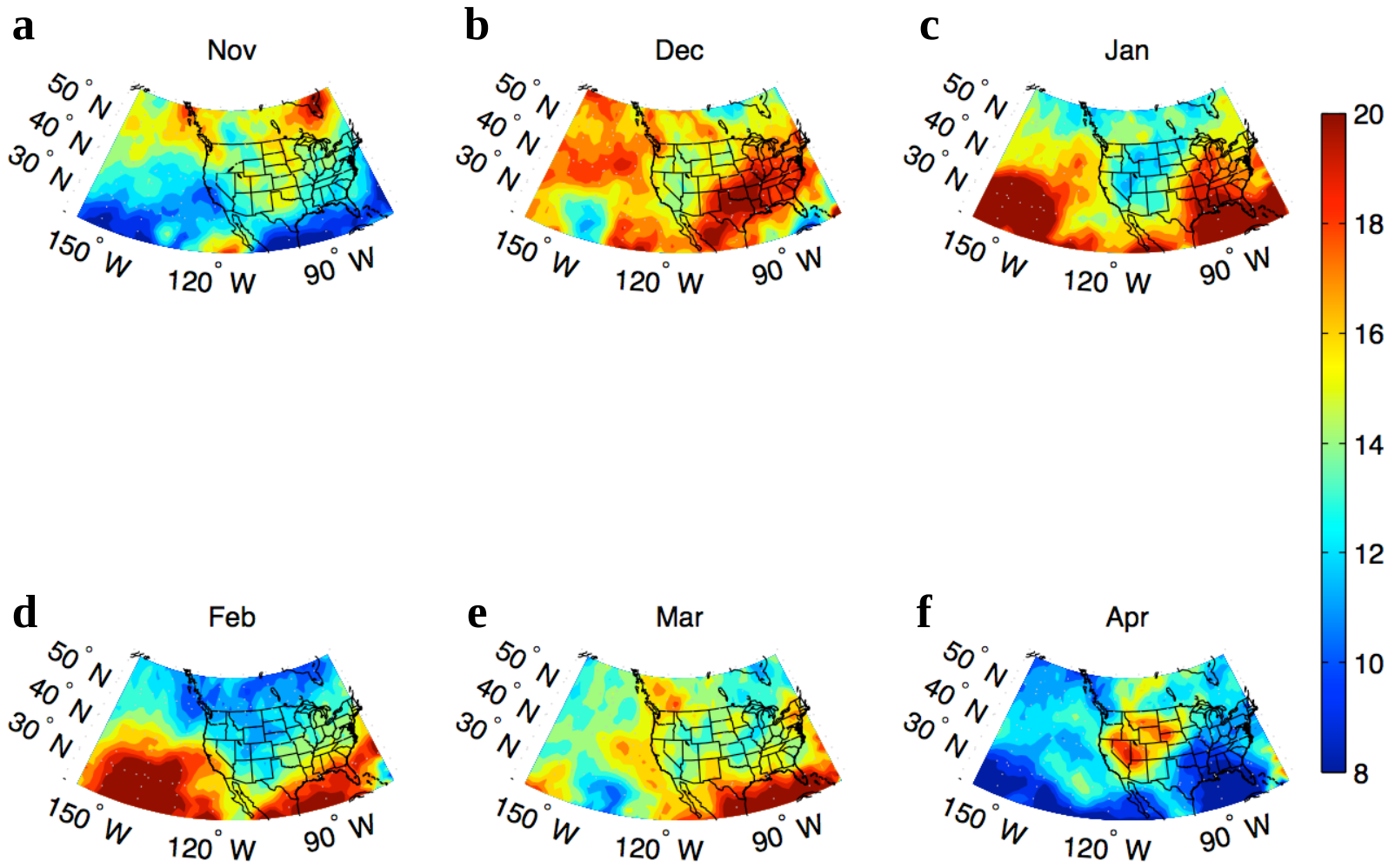

Figure 4.4. Climatological monthly contributions of ascent to the total winter season mean ascent. Color shading represents the percentage of monthly contribution relative to the total.

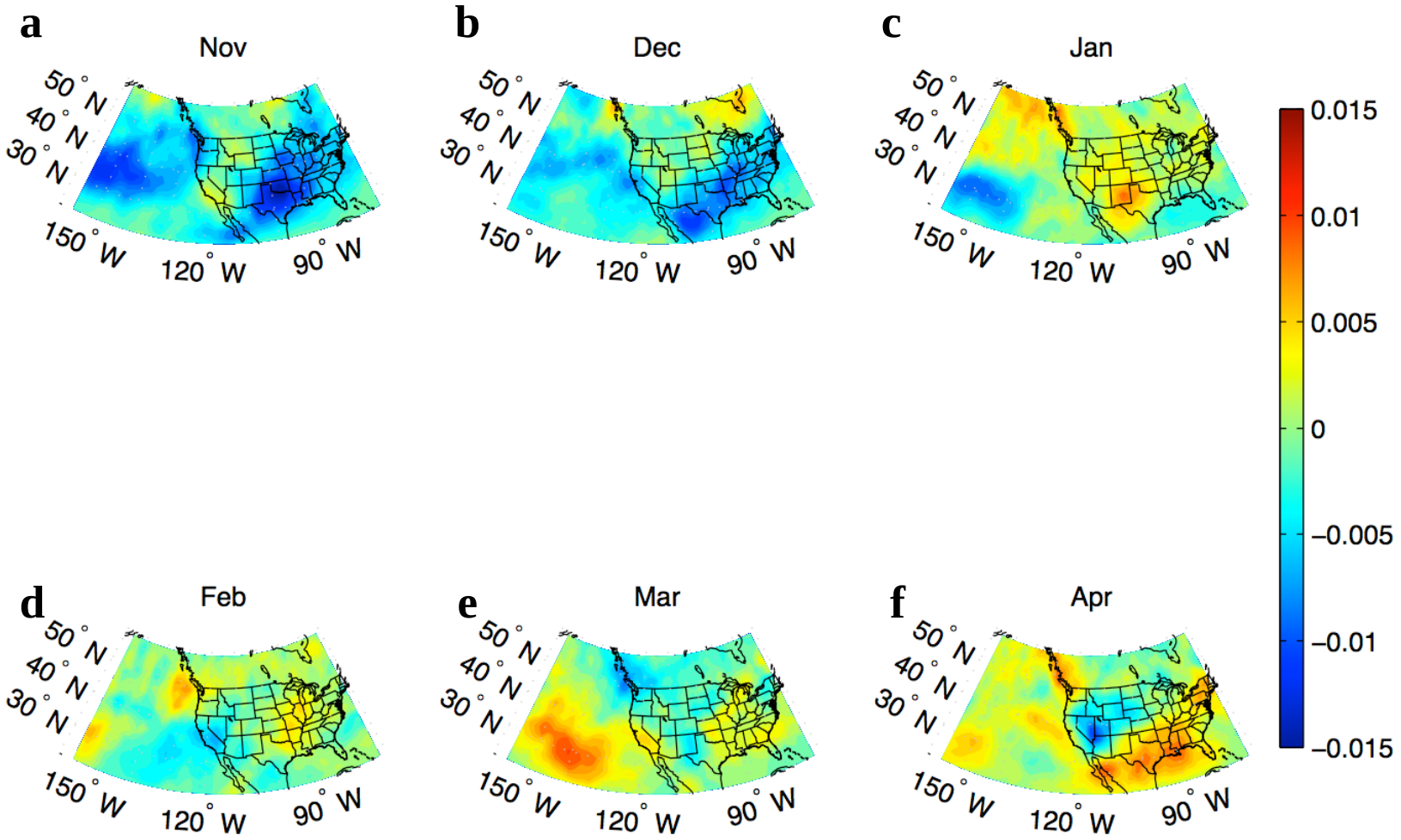

Figure 4.5. Difference between mean ascent (Pa s^{-1}) during a month with that of the previous month. Negative (positive) values indicate relative increases (decreases) in ascent.

and shifts southward along the west coast (Fig. 4.5a). This southward shift continues from November to December with increased ascent during December particularly evident in northern California and along a broad swath from Northern Mexico across the eastern US (Fig. 4.5b). Ascent generally decreases, during January (Fig. 4.5c) throughout much of the domain except over the eastern Pacific Ocean and Gulf of Mexico, locations that exhibit climatologically low mean ascent (Fig. 4.1a). Evident in all seasonal metrics, February storms bring a strong increase in ascent over the southwestern US and adjacent oceanic waters (Figs. 4.3d, 4.5d), and contribute strongly to the seasonal total ascent (Fig. 4.4d), especially for coastal California. The strong increase (decrease) in storminess over California (Pacific Northwest) from January to February reverses over the next month (Figs. 4.5d, 4.5e).

Ascent is strongly diminished nearly everywhere in the domain during April except for an exceptionally strong and spatially coherent increase in upward motions centered over the Great Basin and extending northeast into the high plains of Wyoming, western South Dakota and Nebraska (Figs. 4.3f, 4.5f). Locally, this strong increase also provides a large contribution to the seasonal total ascent of nearly 20% (Fig. 4.4f). This April peak in synoptic-scale ascent corresponds well with the seasonal intensification in precipitation and cyclone activity in the intermountain west (Klien et al. 1968, JM).

The month during which each grid point experiences its peak mean ascent is shown in Fig. 4.6, providing a more concise summary of the seasonal cycle. The spatial distribution of these seasonal peaks shows remarkably coherent regional structures that agree well with synoptic experience. For example, peak ascent during November-December is evident over British Columbia and the North Pacific as well as over much of

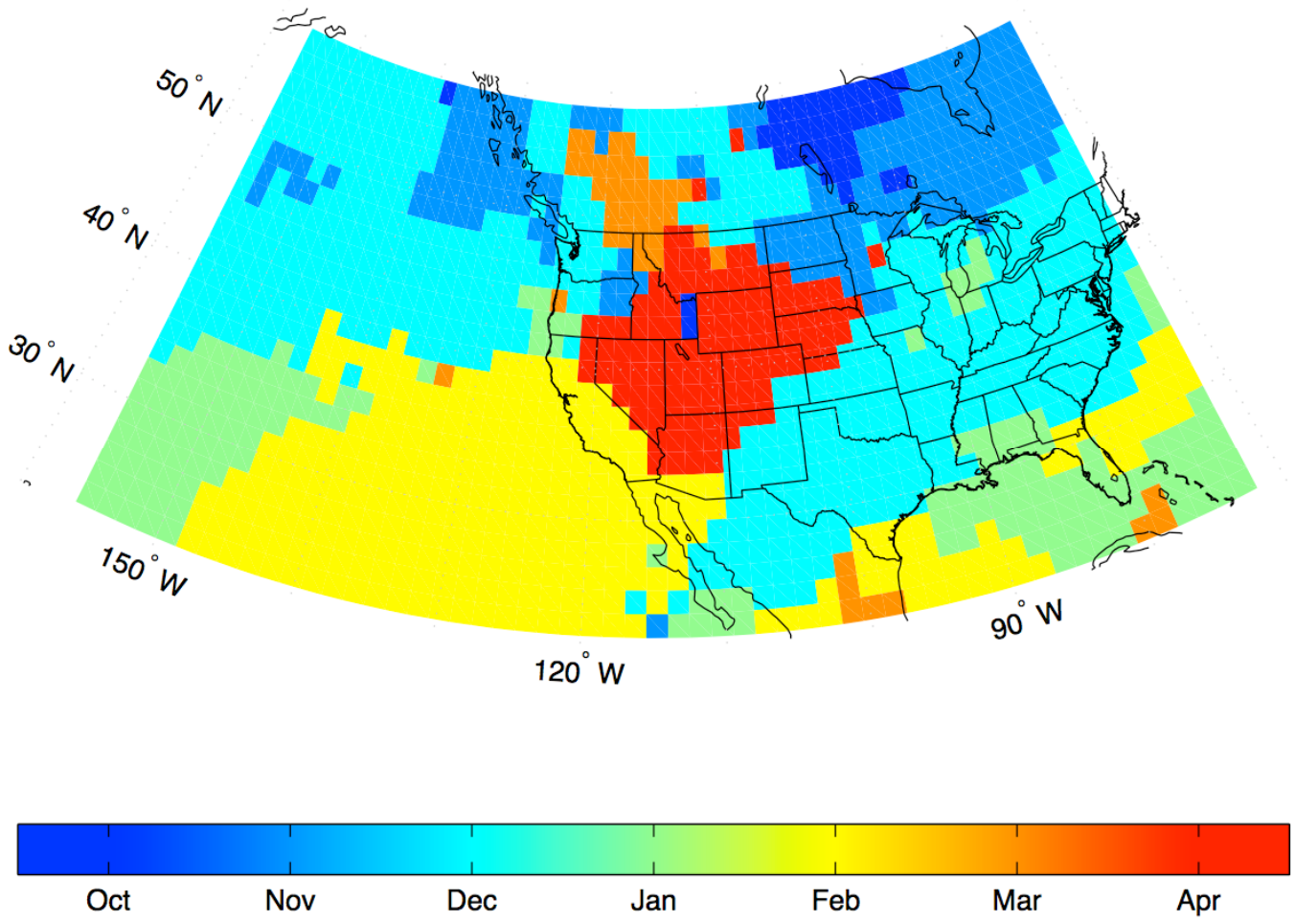

Figure 4.6. Month of maximum ascent.

the eastern US and Canada. In contrast, California and adjacent regions of the Pacific experience a seasonal peak during February, Alberta experiences a peak during March, and the interior mountain west has the greatest ascent during April. This early spring maximum for the North American cordillera is a conspicuous feature, the origins of which warrant future investigation. It should be noted that the amplitude of the seasonal cycle, which is not shown, is particularly weak over northern interior portions of the domain such as Alberta.

Interannual Variability of Synoptic-Scale Ascent

As described in Chapter 2, standardized anomalies for each of the 19 cool seasons were calculated for each grid point by removing the climatological mean ascent and dividing by the year-to-year standard deviation. From the correlation matrix derived from the 19 cool-season standardized anomaly fields, two dominant coherent modes of interannual variability were determined using principal component analysis (Fig. 4.7). The first principal component and its associated eigenvector, or time series, explains 20% of the interannual variance in ascent. Its spatial pattern reflects strong out-of-phase year-to-year variations between regions equatorward and poleward of the band of greatest climatological mean ascent (Fig. 4.1a). The second principal component and eigenvector explain 13% of the interannual variance (Fig. 4.1b) and exhibits multiple centers of action, the strongest of which is centered near 40^{o}N,130^{o}W and spans much of the east Pacific. The small number of years in this data set precludes evaluating higher modes.

Interpretation of these two principal components is facilitated by superimposing the Multivariate El Nino Index (MEI) that represents the phase of ENSO (Wolter and

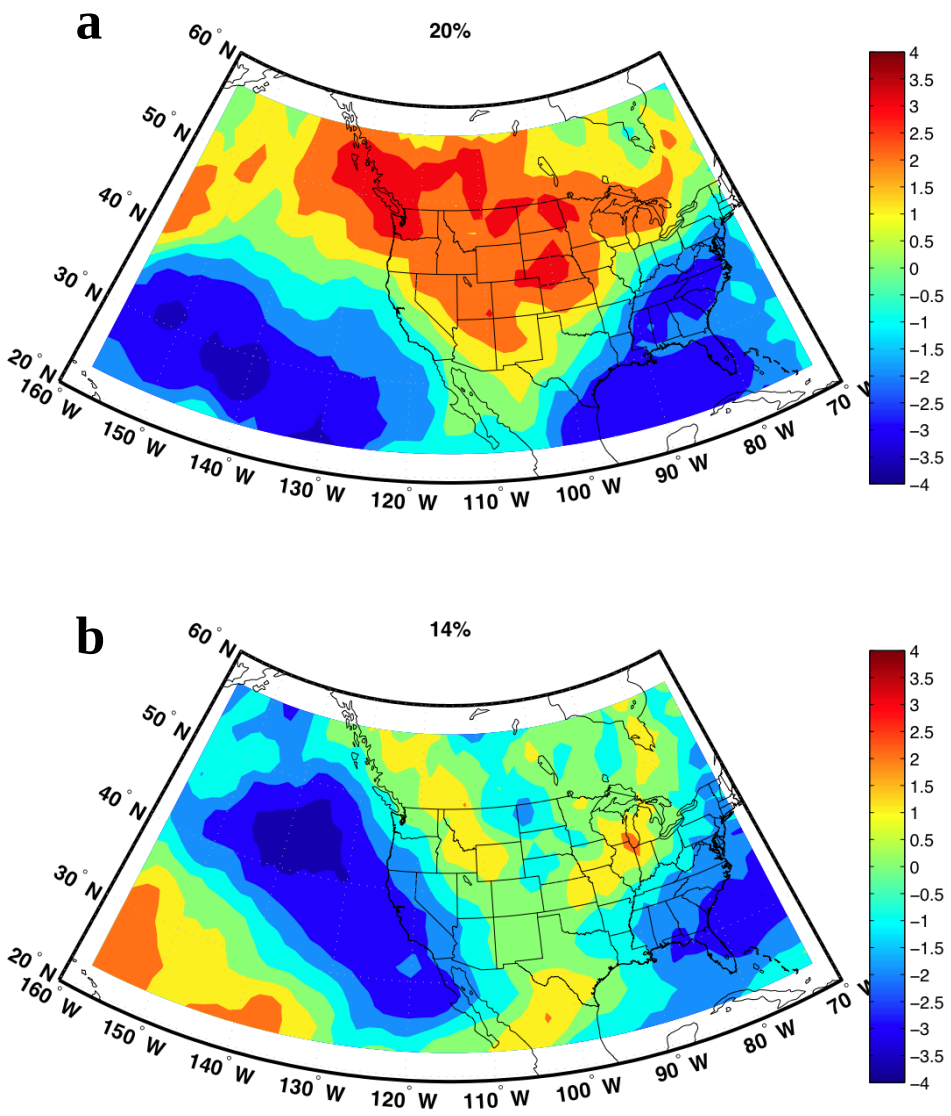

Figure 4.7. Leading modes of interannual variability. (a) First principal component and explained variance. (b) Second principal component and explained variance. Cool (warm) colors indicate regions of enhanced (diminished) ascent during positive phases. The opposite is true for negative phases of these patterns.

Timlin 1998) on the first eigenvector, or time series, (Fig 4.8a) and superimposing a measure of the Pacific/North American index (Wallace and Gutzler 1981) on the second eigenvector (Fig. 4.8b). The first eigenvector had one of its largest positive amplitudes during the 1998 El Nino, which reflects a spatial anomaly pattern of enhanced ascent along 30^{o}N over the Pacific Ocean and diminished ascent over the Pacific Northwest, British Columbia and much of the interior of the United States. Alternatively, increased ascent in the latter regions would be expected to have taken place during the 2008 La Nina cool season. Hence, synoptic ascent is shifted southward into a more zonal pattern during positive phases of the first principal component while the sinusoidal nature of the mean synoptic ascent is accentuated during negative phases.

It is clear from Fig. 4.8a that there is a strong association between the first eigenvector of interannual variability in synoptic-scale ascent and ENSO, with a linear correlation of r=0.76 between them. This correlation is quite large (even taking into consideration the limited number, ~7, of degrees of freedom in this sample), and is significant at the 95% level. Hence, this relationship reinforces the known relationships between positive ENSO phases forcing a southward displacement of the storm track along the west coast of the United States combined with diminished synoptic-scale ascent over the Pacific Northwest (Myoung and Deng 2009; Wettstein and Wallace 2010). For negative phases of ENSO, the opposite holds true, with enhanced synoptic lift in an amplified wave pattern across the North American continent. Composites of the synoptic-scale ascent during the three strongest positive and negative ENSO years within this 19 year sample are presented as well in Fig. 4.9. Similarly, positive ENSO phases favor a strengthened and eastwardly elongated Pacific jet stream while the negative

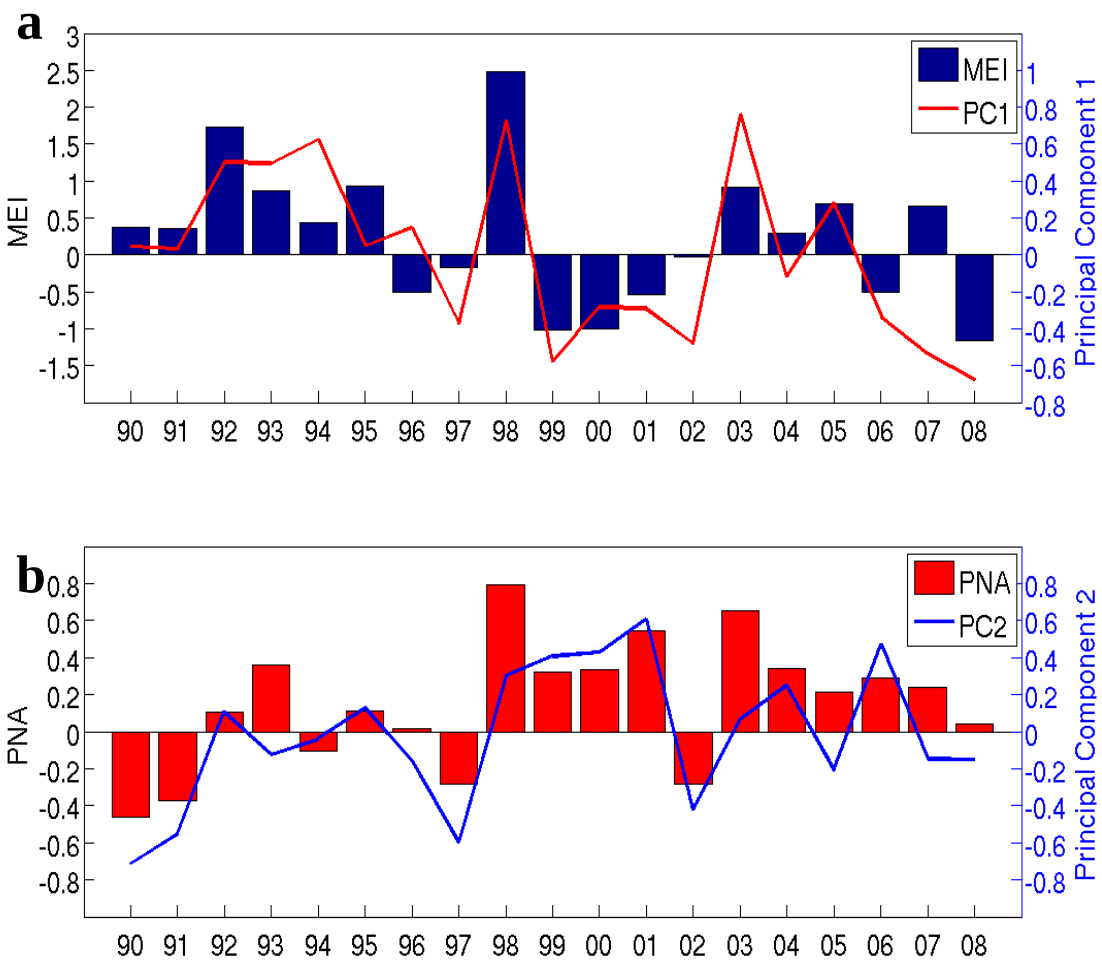

Figure 4.8. Interannual variation in principal components, MEI, and PNA (a) Time series for the MEI (blue bars, left ordinate) and that of the first principal component (red line, right ordinate). (b) Time series for the PNA (Red bars, left ordinate) and that of the second principal component (blue line, right ordinate).

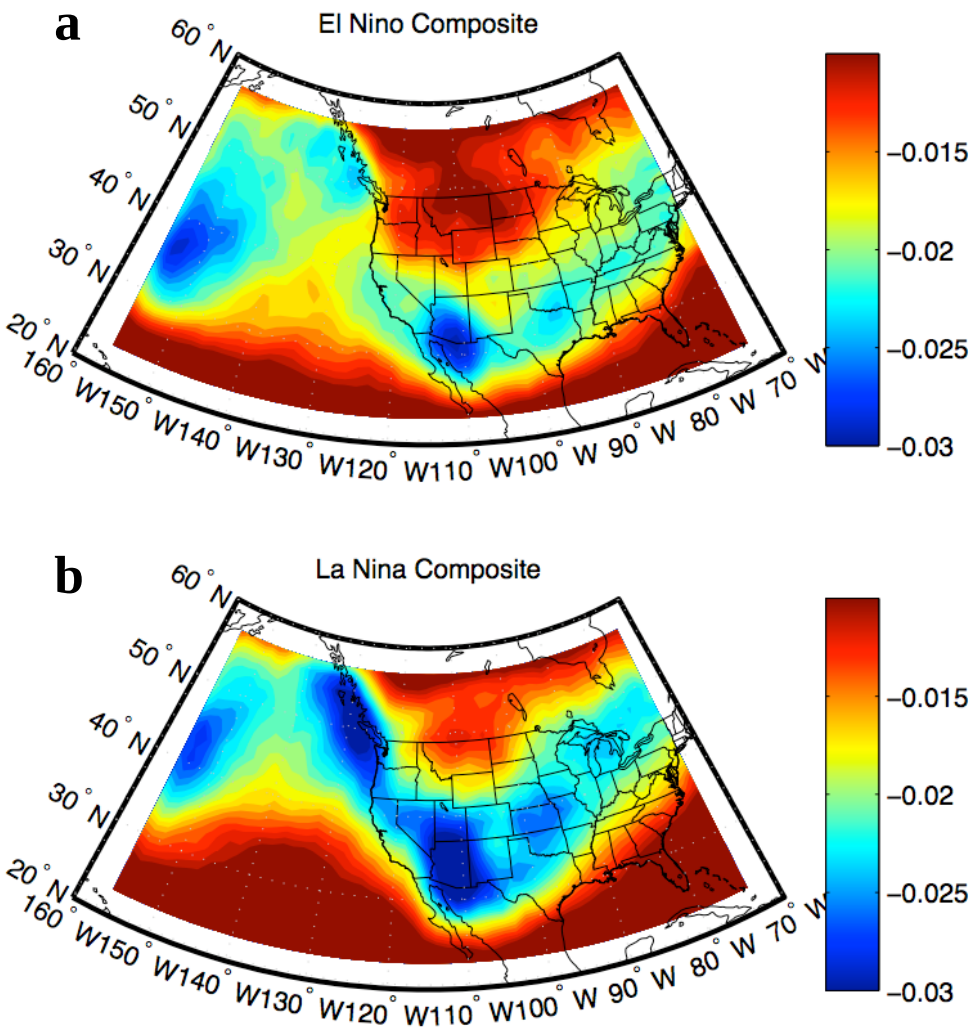

Figure 4.9. Winter season composites of ascent for the three strongest (a) El Nino (1992, 1995, 1998) and (b) La Nina seasons (1999, 2000, 2008).

ENSO phases are associated with an amplified climatological wave pattern and a more variable eastern Pacific jet stream.

The temporal relationship between the second eigenvector (time series) and the PNA index is also strong (r=.80), which is significant at the 99% confidence level assuming ~7 degrees of freedom. Spatially, the anomaly pattern of the second principal component (Figure 4.7b) also bears similarity to the Rossby standing wave pattern of mid-tropospheric height anomalies associated with the PNA (Wallace and Gutzler 1981; Wettstein and Wallace 2010). However, the interpretation of this relationship is complicated by the known link between the PNA and ENSO (r=0.57 during the study period), which is not seen between the second principal component and the MEI, which share virtually no variance in common. This is not altogether unexpected as the first and second eigenvectors are constrained to be orthogonal in time. Caution must again be invoked in interpreting these results due to the limited sample size, with further investigation required to understand these relationships in more detail.

CHAPTER 5

DISCUSSION

Storm tracks across western North America were defined in the previous chapter in terms of the climatological mean occurrence and intensity of synoptic-scale ascent. Additional context for these results are presented here based on prior research. In addition, year-to-year variability of the storm tracks is related to variability in precipitation.

While details of the ascent-based methodology used in this work are novel, HH previously explored 500 hPa omega using tracking and variance approaches (see Chapter 1). It is not surprising that a number of their omega based storm track features differ from those presented in the previous chapter, since the approach adopted here focuses only on synoptic-scale omega, filters most orographic ascent, and does not require track smoothness and duration criteria. For example, the HH omega variance exhibits a weak wave in an otherwise zonal storm track whereas the present study suggests a more amplified sinusoidal track. On the other hand, the HH negative omega (ascent) tracking statistics do show a more meridionally amplified pattern across western North America which features a region of high track density along the British Columbia and US northwest coastlines which then extends south-southeast towards Arizona. This distribution corresponds well with some of the regions of high climatological mean

ascent seen in Fig. 4.1a. However, the correspondence deteriorates proximal to the continental divide, where HH track statistics show zonally minimized values in track density contrasting with the strong southern connection in the ascent based storm track shown in this study.

The present study's ascent-based storm track exhibits greater correspondence with mid- and upper-tropospheric trough and vorticity climatologies. Despite using different metrics, HK, LNG, and the present study all depict a sinusoidal primary storm track and a weak secondary storm track across the Canadian Rockies. The location of local maxima and minima within the storm track also corresponds relatively well, although both the HK and LNG tracks and maxima appear displaced westward of those in this study near California.

The similarity of mid-tropospheric vorticity based measures and synoptic-scale ascent is likely a consequence of the role of vorticity in the traditional omega equation:

$$\left(\nabla^2 + \frac{f_0}{\sigma}\frac{\partial^2}{\partial \mathrm{p}^2}\right)\omega = \underbrace{\frac{f_0}{\sigma}\frac{\partial}{\partial p}\left[V_g \cdot \nabla\left(\frac{1}{f_0}\nabla^2\Phi + f\right)\right]}_{\boldsymbol{A}} + \underbrace{\frac{1}{\sigma}\nabla^2\left[V_g \cdot \nabla\left(-\frac{\partial\Phi}{\partial p}\right)\right]}_{\boldsymbol{B}} \qquad (5.1)$$

In place of the divergence of the Q-vector, the two terms on the RHS represent (**A**) the vertical differential advection of absolute vorticity and (**B**) the horizontal Laplacian of temperature advection (both vorticity and temperature are expressed in terms of geopotential, Φ). The Q-vector form shown in (2.6) is generally favored because the two RHS terms above often tend to cancel one another. However, the RHS can be dominated in some synoptic situations by the vorticity advection term, which itself tends to be

dominated by vorticity advection aloft. For example, consistent with differences between the location of vorticity centers and vorticity advection, the Arizona ascent maximum found in this study is east of the vorticity maxima of HK, which, in turn, is east of the Eulerian Centripetal Acceleration (ECA) maximum of LNG. Equivalent barotropic cutoff low pressure systems that are frequently found in the south eastern Pacific (Bell and Bosart 1989) may contribute strongly to the LNG and HK maxima due to strong curvature and slowly moving vorticity centers, yet have less effect on ascent statistics.

Since the frequency of occurrence of events depends to a degree on the thresholds used to define the events, it is not surprising that the HK vorticity features are estimated to occur roughly 20-30% of the time within the storm track in contrast to 12-20% of the time for synoptic-scale ascent. However, the greater occurrence of vorticity features relative to synoptic-scale ascent may also arise from considering the complete RHS of the omega equation. If horizontal vorticity gradients are weak, the vertical derivative term is not strong, or temperature advection is relevant, then the presence of a vorticity center may have reduced impact on rising motions. The present study likely provides a more stringent restriction for assessing the relevance of synoptic-scale storms.

In light of the similarities detailed above and computational ease, it may be tempting to assume that adequate storm tracks could be produced using the advection of absolute vorticity at 500 hPa or convergence of the Q-vector. To illustrate limitations for that approach, Fig. 5.1 shows the climatological mean distribution of the convergence of the Q-vector as opposed to the climatology obtained using the fully-integrated omega solution (Fig. 4.1a). Overall, higher mean values of convergence of the Q-vector are located further north than the mean values of omega, as a result of the latitudinal and

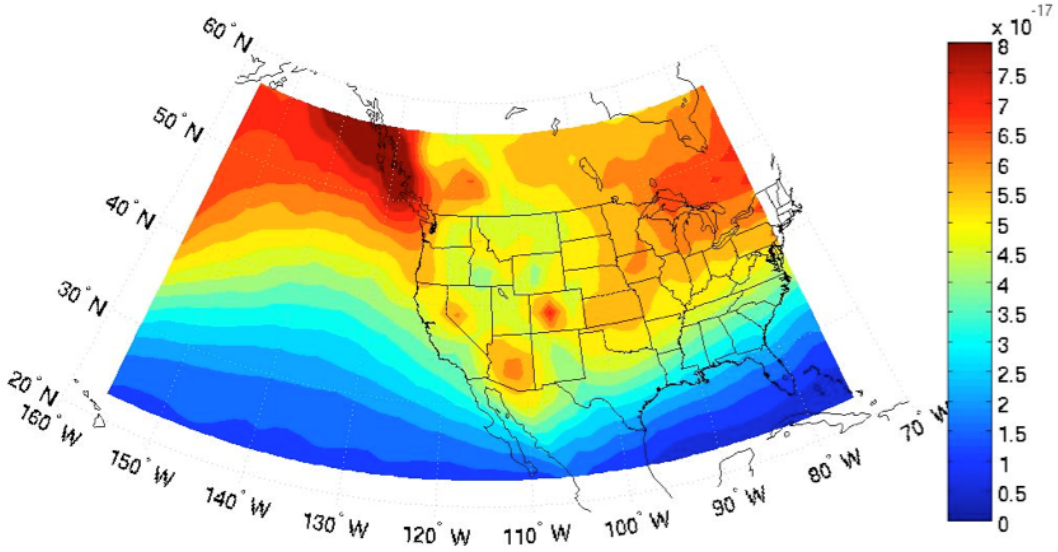

Figure 5.1. Climatological mean distribution of $-2\nabla_p \cdot \vec{Q}_\psi$ (K m^{-2} s^{-1}).

stability dependence of omega. As discussed in Chapter 2, ascent will be greater in regions of lower latitude or weaker stability for a given local source of $-2\nabla\cdot Q$. Although Elbern et al. (1998) employed a strong positive $-2\nabla\cdot Q$ constraint to identify tropopause folds, their resulting climatology is quite similar to the ascent-based storm track and does not suffer from a northern bias. The requirement of a collocated depression of the dynamic tropopause may help to overcome the sensitivity to latitude.

Cyclones

This climatology of mid- and upper-tropospheric synoptic-scale ascent exhibits considerable similarity with some surface cyclone climatologies. Three subsets of cyclones, Alberta Clippers, Rocky Mountain cyclones, and Great Basin cyclones, all seem to be well represented in the ascent based storm track.

Thomas and Martin (2007) provided a comprehensive climatology of the Alberta Clipper, demonstrating both the archetypal storm evolution (including inferred vertical motion) and the preferred tracks of these systems. Clippers tend to be weak systems originating from upstream Pacific vorticity maxima that subsequently traverse the mean ridge and Canadian Rockies. The common feature, of course, is the spin up of low level vorticity in the lee trough region and then the disturbance amplifies vertically and moves with westward tilt and stronger cyclonic relative vorticity observed at 500 hPa later in its life cycle. Accordingly there is typically an increasing $-2\nabla\cdot Q$ signal aloft as the systems progress east. This evolution corresponds well with the details of the mean ascent northern track in Fig. 4.1a. Subjective analysis of seasonal animations of ascent suggests many of the features that contribute to the northern track propagate from the Gulf of

Alaska, east across the Canadian Rockies, and then across the high plains of Canada consistent with the Alberta Clipper morphology. Additional contributions to this portion of the storm track from more northern sources, as well as retrogressing features related to deep circulations near the Great Lakes, are also observed.

Rocky Mountain cyclones, which have a strong genesis maximum in the lee of the Rocky Mountains near the southeastern corner of Colorado (Klein et al. 1968; Rietan et al. 1972; Zishka and Smith 1980; HH; JM) also appear to be present in the ascent-based storm track. Local maximum C, in Fig. 4.1a, is found just downstream of the cyclone density maximum which is suggestive of similar dynamics to those observed with the Alberta Clipper. In general, ascent maxima are likely to be found downstream of cyclogenesis maxima due to the timescales required for development as well as the tendency for ascent to be displaced to the east of the trough axis or cyclone center.

Great Basin cyclones have been found to occur most frequently in a region anchored on the lee side of the highest portions of the Sierra Nevada mountains and extending northeast across Nevada towards the Great Salt Lake Basin in Utah (JM). Examining the fetch of high mean ascent and ascent frequency upstream of maximum B, in Fig. 4.1a, it is apparent that these regions of cyclone occurrence are found beneath regions of high climatological ascent. Furthermore, JM finds a dramatic increase in cyclone occurrence for the Great Basin province during the month of April, the same month for which ascent maximizes across the region (Fig. 4.6). These results are further supported by Whittaker and Horn (1981), who showed a maximum in great basin cyclogenesis during April.

Arizona Ascent Maximum

The Arizona maximum in mean synoptic ascent, maximum B in Fig 4.1a, may strike some readers as a strange or even erroneous feature of this study, since it coincides with a region of limited precipitation and cloud cover. This disparity was also documented by Rose and Lin (2003) as a very low temporal correlation at 6-hour intervals between precipitation rate and 700 hPa vertical motions for the southwestern US. However, as the occurrence of precipitation requires moisture as well as lift, it seems reasonable to postulate that moisture is the limiting factor. Exploring this relationship, a composite of all 6-h periods with ascent centered on maximum B (Fig. 5.2a) shows that the core of rising motion coincides with relative humidity (RH) in the range of 40%. This low RH coincident with the rising motion differs markedly from systems elsewhere in the domain, such as the Pacific Northwest (Fig. 5.2b), where RH near 60% is typical throughout regions of ascent. For reference, the mean RH at 600 hPa during ascent events is shown for the entire domain in Fig. 5.3b relative to the climatological mean RH at that level during all 19 cool seasons (Fig. 5.3a). More northern and elevated locations are much more likely to possess air near saturation in concert with ascent, thus making precipitation a more likely outcome. Not surprisingly the difference between the climatology of RH for all cool season days (Fig. 5.3a) and that during only ascent events (Fig 5.3c) shows that rising motions nearly always bring air closer to saturation, though some spatial variability in strength of this relationship exists. For the southwestern US, ascent does in fact increase RH; however, the climatological base state is sufficiently dry that saturation is hard to attain.

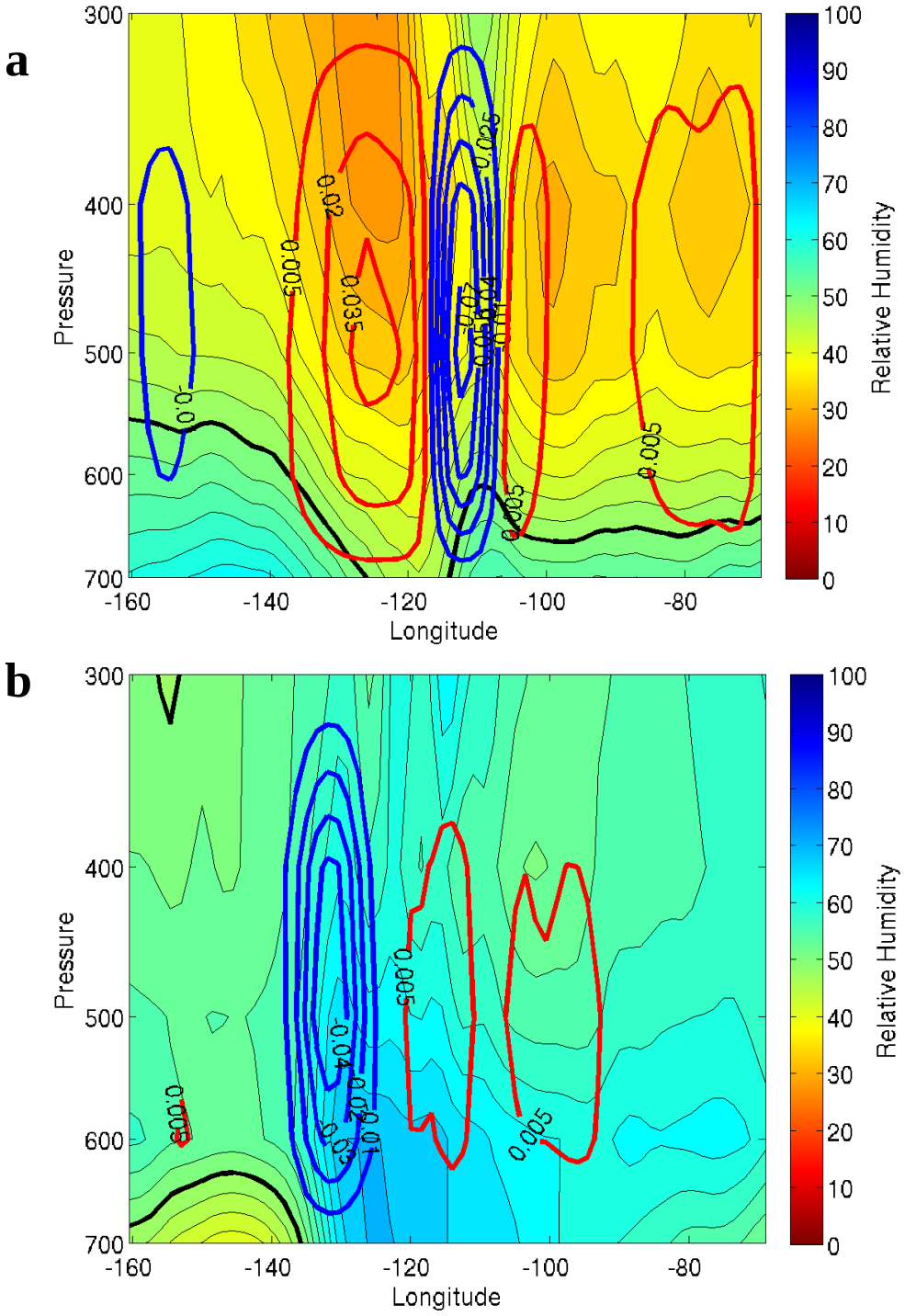

Figure 5.2. Composite zonal cross sections for (a) storms contributing to the Arizona maximum (Max. B in Fig. 4.1a) and (b) those contributing to the Pacific Northwest Maximum (Max A in Fig. 4.1a). Shading indicates composite storm relative humidity with cool (warm) colors indicating higher (lower) relative humidity. The heavy black contour represents 50 % relative humidity. Blue (Red) labeled contours indicate ascent (decent) in Pa s^{-1}.

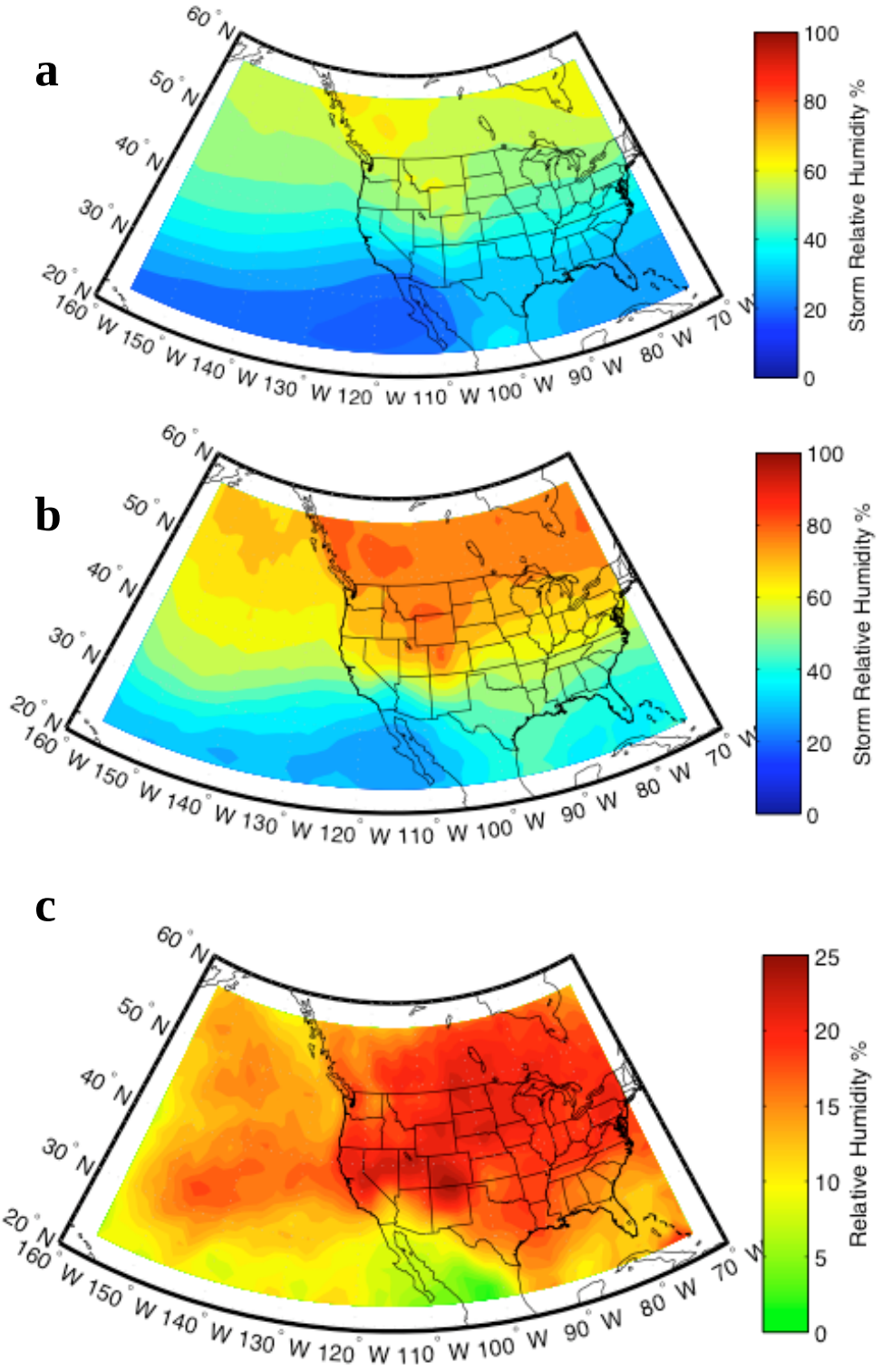

Figure 5.3. Relative humidity analysis.(a) Climatology of winter season relative humidity. (b) Climatological distribution of relative humidity during ascent events. (c) Difference between ascent relative humidity and climatology

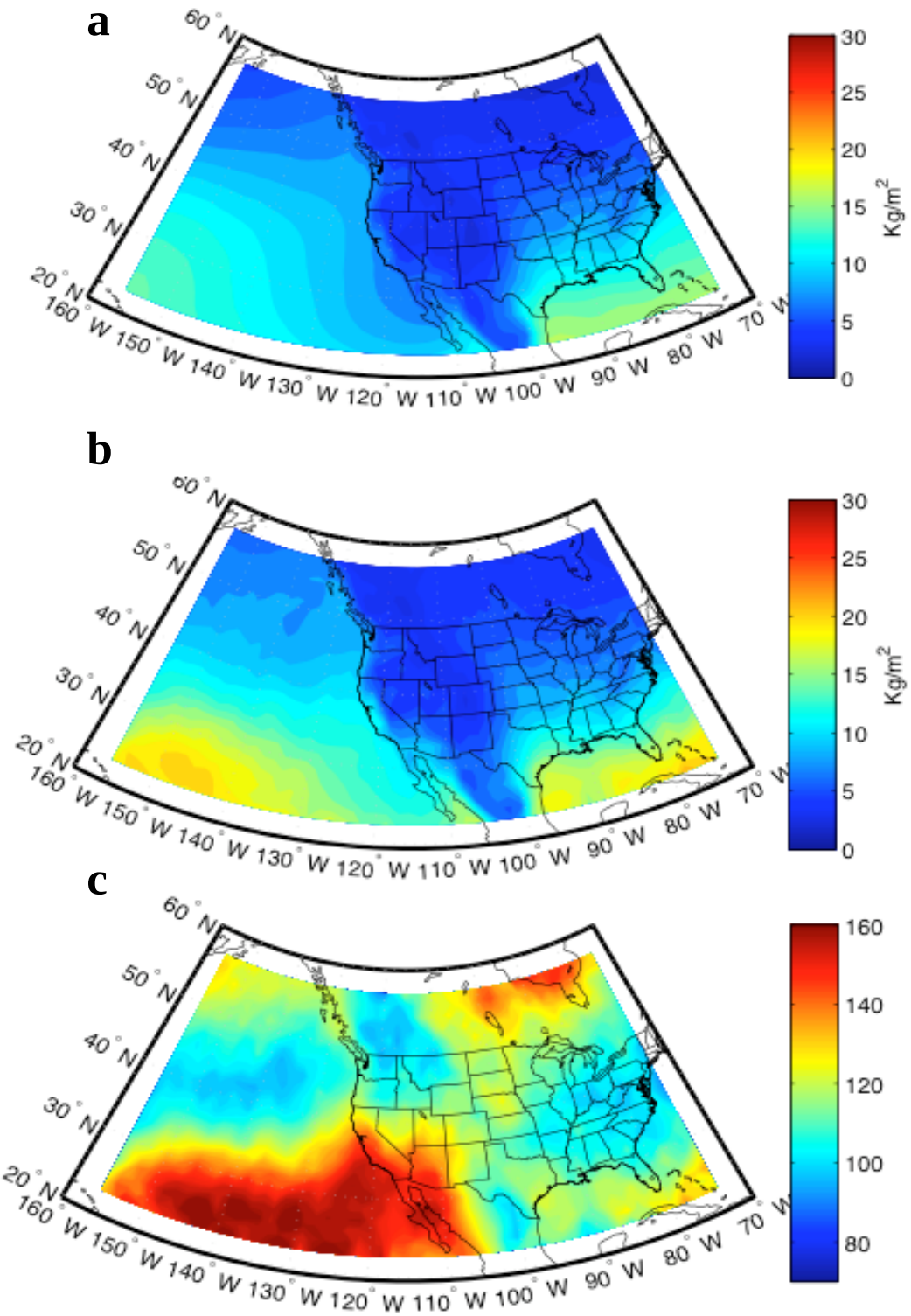

Figure 5.4. Column total water (TW) analysis. (a) Climatology of winter season column TW. (b) Climatological distribution of TW during ascent events. (c) Percent of normal TW associated with ascent events.

While RH is an important consideration for the initiation of precipitation processes, column integrated total water (TW), which is the sum of water vapor and cloud condensate, may modulate the amount of precipitation that is possible. The climatology and storm related anomalies in TW are documented in Fig. 5.4. Interestingly, some regions within the primary storm track experience reductions, or neutral anomalies of TW, in the presence of ascent. To the contrary, southern portions of the domain tend to see significant increases in TW; however such anomalies are only relevant once saturation is achieved.

Precipitation Variability

Appreciating that ascent by itself does not lead to precipitation, it is still intriguing to explore the links between interannual variations in synoptic-scale ascent and the variability in regional precipitation. An independent and higher resolution representation of monthly precipitation is obtained from the Parameter-elevation Regression on Independent Slopes Model (PRISM; Daily et al. 1994). This gridded data set provides an elevation and slope sensitive estimation of precipitation at a resolution of 30-arc-seconds for the US domain based on point observations and observed climatic distributions. Monthly totaled values summed for October-April periods are used in this study. The PRISM precipitation grids were processed in a manner identical to that used for ascent in order to obtain standardizes anomalies for each of the 19 cool seasons at each grid point.

Regressing the time series of mean ascent (red line in Fig 4.8a) with the time series of PRISM precipitation standardized anomalies at each grid point yields a now familiar north-south dipole pattern of ENSO-related precipitation variability for the

western US (Fig. 5.5a). Assuming as few as 7 independent events, the correlation between seasonal anomalies of ascent and precipitation should be viewed with some caution. Positive (negative) correlations are found for the arid southwest (Pacific Northwest). Interesting local exceptions to this pattern exist, dominated by the tendency for low elevation arid (high elevation moist) regions to be positively (negatively) correlated with the PC1 time series. For the eastern portions of the US, positive correlations are found across the southeast, with negative correlations across the upper Mississippi and Ohio River basins. A similar pattern of precipitation anomalies arises independently as the third principal component of PRISM precipitation variations computed from the 19 x 19 correlation matrix between the cool season standardized anomalies (Fig. 5.5b). Taking into consideration the limitations imposed from the small sample size, the associated principal component time series has a weaker correlation (r~=-.62) with the MEI than does the related first principal component time series of synoptic ascent (r~= -.76), which may suggest that there is a more direct ENSO control on storm track than on the amount of precipitation. This disparity may again have to do with available moisture modulating the productivity of synoptic-scale ascent.

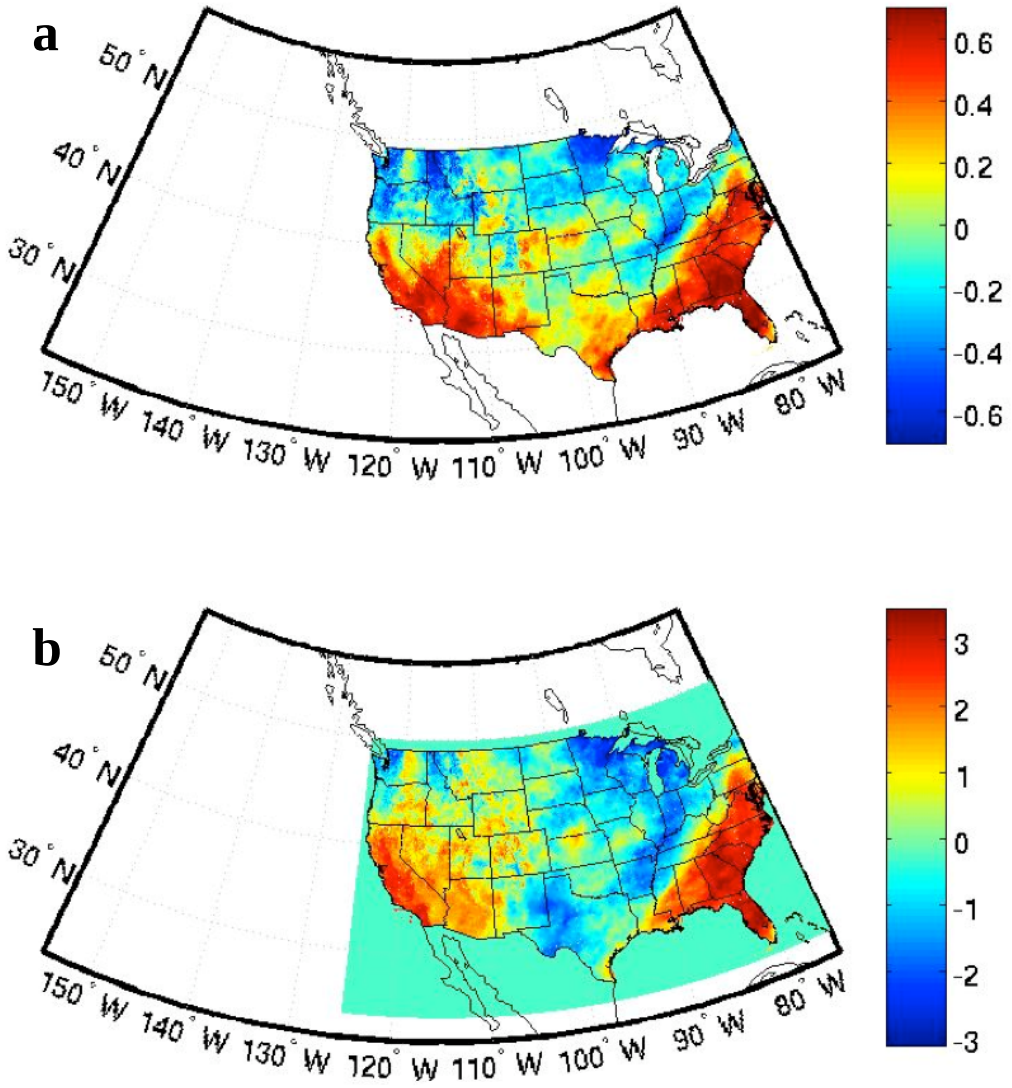

Figure 5.5. Variability in precipitation associated with variation in synoptic-scale ascent. (a) Linear correlation coefficients between the first principal component time series of ascent and the grid point time series of standardized PRISM precipitation anomalies. (b) The third principal component of the PRISM interannual variations.

CHAPTER 6

CONCLUSIONS

This study examines the position and variability of storm tracks across western North America. A dynamically filtered and physically relevant method was introduced wherein the climatological distribution of ascent was shown to be representative of storm tracks. An alternative balance version of the omega equation was used to diagnose the component of ascent associated with synoptic-scale motions while dynamically filtering poorly-resolved mesoscale contributions, such as terrain forced flows. The maximum values of ascent among 5 mid-tropospheric levels were retained at each 6-hour interval over 19 cool seasons. Animations of the maps of ascent were examined subjectively during all seasons and a case study was used to evaluate the sensitivity of the results to the technique. Summary ascent statistics over months, seasons, and the entire 19-year period yield a measure of the propensity of a location to experience synoptic-scale disturbances. Locations exhibiting high mean ascent and ascent frequency are thus said to be storm tracks.

The climatological mean ascent-based storm track was found to occupy a sinusoidal belt across western North America. Variations in the position of the storm track were shown to be related to the phase of ENSO, with El Niño (La Nina) winters favoring a more zonal (amplified) and southern (northern) storm track. The relationship

between variations in ascent and those in precipitation were observed to be modulated by available moisture and the saturated state of the atmosphere. The ascent based storm tracks were also shown to be consistent with elements of previous lower-, mid-, and upper-tropospheric storm track studies.

Remaining research questions pertain to the large scale dynamics that contribute to the observed structure of the storm track. In particular, the strong southward displacement of high mean ascent along the US west coast is a peculiar feature as is the ascent minima proximal to Montana. Additionally, the tendency for storms that are displaced south from the mean pathway to exhibit stronger rising motion poses questions about the structure and dynamics of these systems. The 'Tax Day Storm' case examined herein, suggests that idealized modeling studies examining the phase locking between upper level PV anomalies and surface thermal waves may yield insights into the evolution of storms in regions of complex topography.

While the sample size of 19 seasons is a limiting factor to reach conclusions about recent year-to-year variations, this study has demonstrated that the analysis approach could easily be adapted to examine changes in storm tracks between present-day and future climate simulations. Since climate models at the present time cannot resolve the terrain of the western US with sufficient fidelity to simulate precipitation processes accurately, this method may help to provide a linkage between anthropogenic changes and regional climate variations in synoptic-scale ascent and thereby large-scale precipitation patterns.

REFERENCES

Bell, G. D., L. F. Bosart, 1989: A 15-year climatology of Northern Hemisphere 500 mb closed cyclone and anticyclone centers. *Mon. Wea. Rev.*, **117,** 2142-2164.

Blackmon, M. L., 1976: A climatological spectral study of the 500 mb geopotential height of the Northern Hemisphere. *J .Atmos. Sci.,* **33, 1607**-1623.

Clough, S. A., C. S. A. Davitt, and A. J. Thorpe, 1996: Attribution concepts applied to the omega equation. *Quart. J. Roy. Meteor. Soc.,* **122,1943**-1962.

Daly, C., R.P. Neilson, and D.L. Phillips, 1994: A statistical-topographic model for mapping climatological precipitation over mountainous Terrain. *J. Appl. Meteor*., **33,** 140-158.

Davies-Jones, R. P., 1991: The frontogenetical forcing of secondary circulations. Part I: The duality and generalization of the Q vector. *J. Atmos. Sci.,* **48,** 497-509.

Davies-Jones, R. P., 2009: The frontogenetical forcing of secondary circulations. Part II: Properties of Q vectors in exact linear solutions. *J. Atmos. Sci.,* **66,** 244-260.

Dean, D. B., and L. F. Bosart, 1996: Northern Hemisphere 500-hPa trough merger and fracture: A Climatology and Case Study. *Mon. Wea. Rev.*, **124,** 2644-2670.

Dee, D. P., and S. Uppala, 2009: Variational bias correction in ERA-Interim. *ECMWF Newsletter No. 119*.

Dee, D. P., and S. Uppala, 2009: Variational bias correction of satellite radiance data in the ERA-Interim reanalysis. *Quart. J. Roy. Meteor. Soc.*,**135,** 1830-1841.

Dee, D. P., P. Berrisford, P. Poli, and M. Fuentes, 2009: ERA-interim for climate monitoring. *ECMWF Newsletter No. 119*.

Durran, D. R., and L. W. Snellman, 1987: The diagnosis of synoptic-scale vertical motion in an operational environment. *Wea. Forecasting,* **2,** 17-31.

Elbern, H., J. Hendricks, and A. Ebel, 1998: A climatology of tropopause folds by global analyses. *Theor. Appl. Climatol.,* **59,** 181-200.

Hakim, J. G., 2000: Climatology of coherent structures on the extratropical tropopause. *Mon. Wea. Rev.,* **128,** 385-406.

Horel, J. D. 1984: Complex principal component analysis: theory and examples. *J. Climate Appl. Meteor.,* **23**, 1660-16673.

Hoskins, B. J., I. Draghici, and H. C. Davies, 1978: A new look at the ω-equation. *Quart. J. Roy. Meteor. Soc.*,**104,** 31-38.

Hoskins, B. J., and M. A. Pedder, 1980: The diagnosis of middle latitude synoptic development. *Quart. J. Roy. Meteor. Soc.*,**106,** 707-719.

Hoskins, B. J., M. E. McIntyre, and A. W. Robertson, 1985: On the use and significance of isentropic potential vorticity maps. *Quart. J. Roy. Meteor. Soc.,* **111,** 877-946.

Hoskins, B. J., and K. I. Hodges, 2002: New perspectives on Northern Hemisphere winter storm tracks. *J. Atmos. Sci.,* **59,** 1041-1061.

Jeglum, M. E., W. J. Steenburgh, T. P Lee, and L.F. Bosart, 2010: Multi-reanalysis climatology of intermountain cyclones. *Mon. Wea. Rev.* in press.

Klein, W. H., D. L. Jorgensen, and A. F. Korte, 1968: Relation between upper air lows and winter precipitation in the western plateau states. *Mon. Wea. Rev.,* **96,** 162-168.

Keyser, D., M. J. Reeder, and R. J. Reed, 1988: A Generalization of Petterson's frontogenesis function and its relation to the forcing of vertical motion. *Mon. Wea. Rev.,* **116,** 762-780.

Keyser, D., B. D. Schmidt, D. G. Duffy, 1992: Quasigeostrophic vertical motions diagnosed from along- and cross-isentropic components of the Q vector. *Mon. Wea. Rev.,* **120,** 731-741.

Krishnamurti, T. N., and L. Bounoua, 1996: *An Introduction to Numerical Weather Prediction Techniques.* CRC Press, Inc., 293 pp

.

Lefevre, R. J., and J. W. Nielsen-Gammon, 1995: An objective climatology of mobile troughs in the Northern Hemisphere. *Tellus,* **47A,** 638-655**.**

Martin, J. E., 2007: Lower-tropospheric height tendencies associated with the shearwise and transverse components of the quasigeostrophic vertical motion. *Mon. Wea. Rev.,* **135,** 2803-2809.

Myoung, B., and Y. Deng, 2009: Interannual variability of the cyclonic activity along the U.S. Pacific coast: Influences on the characteristics of winter precipitation in the western United States. *J. Climate,* **22,** 5732-5747.

Reitan, C. H., 1974: Frequencies of cyclones and cyclogenesis for North America, 1951-1970. *Mon. Wea. Rev.,* **102,** 861-868.

Rose, B. E. J., and C. A. Lin, 2003: Precipitation from vertical motion: A statistical diagnostic scheme. *Int. J. Climatol.,* **23,** 903-919.

Sanders, F., 1988: Life history of mobile troughs in the upper westerlies. *Mon. Wea. Rev.,* **116,** 2629-2648.

Serreze, M. C., M. P. Clark, R. L. Armstrong, D. A. McGinnis, and R. S. Puwarty, 1996: Characteristics of the western U.S. snowpack from SNOTEL data. *Water Resour. Res.,* **35,** 2145-2160.

Simmons, A., S. Uppala, D. Dee, and S. Kobayashi, 2007: ERA-interim: New ECMWF reanalysis products from 1989 onwards. *ECMWF Newsletter No. 110.*

Simmons, A., S. Uppala, and D. Dee, 2007: ERA-interim: New ECMWF reanalysis products from 1989 onwards. *ECMWF Newsletter No. 111*.

Stuart, D. W., 1967: The over-relaxation factor in the numerical solution to the omega equation. *Mon. Wea. Rev.,* **95,** 303-307.

Sutcliffe, R. C., 1947: A contribution to the problem of development. *Quart. J. Roy. Meteor. Soc.,* **73,** 370-383.

Thomas, B. C., and J. E. Martin, 2007: A synoptic climatology and composite analysis of the Alberta Clipper. *Wea. Forecasting,* **22,** 315-333.

Trenberth, K. E., 1978: On the interpretation of the diagnostic quasi-geostrophic omega equation. *Mon. Wea. Rev.,* **106,** 131-137

Uppala, S., D. Dick, S. Kobayashi, P. Berrisford, and A. Simmons, 2008: Towards a climate data assimilation system: status update of ERA-Interim. *ECMWF Newsletter No. 115.*

Wallace, J. M., and David S. Gutzler, 1981: Teleconnections in the geopotential height field during the Northern Hemisphere winter. *Mon. Wea. Rev*, **109**, 784-812

Wernli, H., and C. Schwierz, 2006: Surface cyclones in the ERA-40 dataset (1958-2001). Part 1: Novel identification method and global climatology. *J. Atmos. Sci.,* **63,** 2486-2507.

West, G. L., and W. J. Steenburgh, 2010: Life cycle and mesoscale frontal structure of an intermountain cyclone. *Mon. Wea. Rev.*in press.

Wettstein, J. J., and J. M. Wallace, 2010: Observed patterns of month-to-month storm-track variability and their relationship to the background flow. *J .Atmos. Sci.*, **67**, 1420-1437.

Wolter, K., and M. S. Timlin, 1998: Measuring the strength of ENSO events - how does 1997/98 rank? *Weather,* **53,** 315-324.

Zishka, K. M., and P. J. Smith, 1980: The climatology of cyclones and anticyclones over North America and surrounding ocean environs for January and July, 1950-77. *Mon. Wea. Rev.,* **108,** 387-401.